

# Benchmarking Foundation Models and Parameter-Efficient Fine-Tuning for Prognosis Prediction in Medical Imaging

Filippo Ruffini<sup>a</sup>, Elena Mulero Ayllon<sup>a</sup>, Linlin Shen<sup>b</sup>, Paolo Soda<sup>a,c,\*</sup>,  
Valerio Guarasi<sup>a</sup>

<sup>a</sup>*Unit of Artificial Intelligence and Computer Systems, Department of Engineering, Università Campus Bio-Medico di Roma, Via Álvaro del Portillo, 21, Rome, 00128, Italy*

<sup>b</sup>*College of Computer Science and Software Engineering, Shenzhen University, School of Computer and Software, Canghai Campus, Shenzhen, China*

<sup>c</sup>*Department of Diagnostics and Intervention, Radiation Physics, Biomedical Engineering, Umeå University, Umeå, 901 87, Sweden*

---

## Abstract

Artificial Intelligence (AI) holds significant promise for improving prognosis prediction in medical imaging, yet its effective application remains challenging. In this work, we introduce a structured benchmark explicitly designed to evaluate and compare the transferability of Convolutional Neural Networks and Foundation Models in predicting clinical outcomes in COVID-19 patients, leveraging diverse publicly available Chest X-ray datasets. Our experimental methodology extensively explores a wide set of fine-tuning strategies, encompassing traditional approaches such as Full Fine-Tuning and Linear Probing, as well as advanced Parameter-Efficient Fine-Tuning, methods including Low-Rank Adaptation, BitFit, VeRA, and IA3. The evaluations were conducted across multiple learning paradigms, including both extensive full-data scenarios and more clinically realistic Few-Shot Learning settings, which are critical for modeling rare disease outcomes and rapidly emerging health threats. By implementing a large-scale comparative analysis involv-

---

\*Corresponding author

Email addresses: [filippo.ruffini@unicampus.it](mailto:filippo.ruffini@unicampus.it) (Filippo Ruffini), [e.muleroayllon@unicampus.it](mailto:e.muleroayllon@unicampus.it) (Elena Mulero Ayllon), [llshen@szu.edu.cn](mailto:llshen@szu.edu.cn) (Linlin Shen), [p.soda@unicampus.it](mailto:p.soda@unicampus.it), [paolo.soda@umu.se](mailto:paolo.soda@umu.se) (Paolo Soda), [valerio.guarrasi@unicampus.it](mailto:valerio.guarrasi@unicampus.it) (Valerio Guarasi)

ing a diverse selection of pretrained models, including general-purpose architectures pretrained on large-scale datasets, such as CLIP and DINOv2, to biomedical-specific models like MedCLIP, BioMedCLIP, and PubMedCLIP, we rigorously assess each model’s capacity to effectively adapt and generalize to prognosis tasks, particularly under conditions of severe data scarcity and pronounced class imbalance. The benchmark was designed to capture critical conditions common in prognosis tasks, as variations in dataset size, class distribution, providing detailed insights into the strengths and limitations of each fine-tuning strategy. This extensive and structured evaluation aims to inform the practical deployment and adoption of robust, efficient, and generalizable AI-driven solutions in real-world clinical prognosis prediction workflows.

*Keywords:* Transfer learning; Deep learning; Precision Medicine

---

## 1. Introduction

Artificial Intelligence (AI) has become a transformative wave in medical imaging, widely adopted across specialties such as radiology, oncology, and pathology [1, 2]. Its effectiveness in disease detection, cancer subtype classification, and early screening [3, 4, 5] was particularly evident during the COVID-19 pandemic, which accelerated the development of AI-driven diagnostic tools for chest X-ray analysis [6, 7], highlighting AI’s value in managing large-scale health emergencies [8].

In parallel, prognostic models have seen significant advancements, making use of increasingly sophisticated methods to estimate and anticipate clinical outcomes, such as disease progression and mortality [9, 10]. However, prognosis tasks remain more complex and less explored than diagnostic tasks, primarily due to data-related challenges such as the inherent temporal structure of the data and the limited availability of high-quality annotations or sufficiently large cohorts [11, 12, 13].

Historically, convolutional neural networks (CNNs) have played a central role in medical imaging, particularly for diagnostic tasks, consistently achieving strong performance when pretrained with supervised learning on large-scale natural image datasets (e.g., ImageNet [14]) and subsequently fine-tuned on clinical datasets [15]. Their architectural inductive biases and parameter efficiency made them well-suited to homogeneous datasets typical of diagnostic tasks. These same architectures have been employed also

in prognostic modeling; however, they exhibit clear limitations in this context. In particular, their limited capacity to capture long-range dependencies, coupled with the requirement for full fine-tuning, reduces their suitability for tasks involving temporally structured data, complex prediction objectives, and scenarios with limited sample availability. [16, 17].

As an alternative to supervised pretraining, which requires huge labeling effort to acquire the datasets needed during training, Self-Supervised Learning (SSL) has emerged as a scalable paradigm that reduces or eliminates the need for manual annotations [18, 19]. Prominent SSL methods employed in DINO [20] or CLIP [21] exemplify this shift, leveraging unlabeled data to learn rich representations through contrastive or distillation-based objectives. They demonstrated stronger transferability to out-of-domain tasks and robustness in high-variance clinical settings [22, 23]. This has led to the emergence of Foundation Models (FMs), which use large transformer architectures pretrained on massive unlabeled datasets. Biomedical variants of FMs have been developed to improve alignment with domain-specific tasks [24, 25, 26], yet their application in prognosis prediction remains largely untested.

The limited exploration of foundation models (FMs) in prognosis is primarily driven by the unique challenges associated with prognostic datasets, which often suffer from severe sample scarcity, extreme class imbalance, and temporally evolving clinical targets [27, 28]. Although FMs have demonstrated superior generalization and robust performance across a range of diagnostic and classification tasks, their adoption in prognostic modeling remains constrained. This is largely due to the difficulty of adapting such large-scale models to the noisy, heterogeneous, and temporally structured nature of prognostic data conditions that amplify the limitations of traditional adaptation techniques. Fine-tuning strategies remain widely adopted in this context. However, their effectiveness is often hindered by issues such as domain shift, limited supervision, and poor representation quality in small target datasets. Despite these challenges, such approaches continue to offer a practical solution due to their simplicity and demonstrated utility across a variety of clinical prediction tasks.

To overcome the scalability and data efficiency limitations of full fine-tuning, Parameter-Efficient Fine-Tuning (PEFT) techniques [29, 30] have recently emerged as a promising alternative. Rather than updating all model weights, PEFT methods focus on modifying a small subset of task-specific parameters—such as bias terms [31], low-rank adapters [32], or scaling vectors [33], while keeping the backbone model frozen. This significantly reduces

computational and memory requirements, mitigates overfitting, and enables more scalable and targeted adaptation to diverse prognostic tasks [34, 35].

Moreover, Few-Shot Learning (FSL) has emerged as a complementary paradigm within transfer learning, specifically targeting scenarios characterized by extreme data scarcity. FSL techniques aim to enable models to generalize effectively from only a handful of labeled examples [36, 37]. By leveraging prior knowledge from pretrained models and carefully designed learning strategies, such as meta-learning and prototype-based classification, FSL allows rapid adaptation to new tasks with minimal supervision. Furthermore, the integration of PEFT methods into FSL pipelines has shown to further enhance adaptation efficiency in resource-constrained environments [38], offering a practical and scalable solution for real-world medical AI applications where annotated data is often difficult and costly to obtain.

In this work, we address the limited exploration of foundation models (FMs) and parameter-efficient fine-tuning (PEFT) strategies in medical prognosis. We introduce a structured benchmark to evaluate fine-tuning methods across a diverse set of pretrained models, including both general-purpose (e.g., ResNet, CLIP) and biomedical-specific architectures (e.g., MedCLIP, BioMedCLIP), covering both CNNs and FMs architectures. Our benchmark focuses on COVID-19 chest X-ray (CXR) prognosis as a clinically relevant and standardized use case, supported by public datasets with varying outcome types, sample sizes, and imbalance levels. Specifically, our contributions are as follows:

- **Comprehensive Comparison of FMs and CNNs architectures.** We present a systematic benchmark comparing PEFT techniques against classical fine-tuning strategies, such as Full Fine Tuning (FFT) and Linear Probing (LP), across both CNNs and FMs. The benchmark covers generalist pretrained models (e.g., ResNet18) and medical pretrained models (e.g., PubMedCLIP), applied to prognostic prediction tasks. We highlight which strategies are more robust to data scarcity and class imbalance—two key challenges in prognosis modeling.
- **PEFT applied to FMs in Prognosis Tasks.** While CNNs have been extensively studied for medical imaging, the use of FMs in prognosis prediction remains underexplored. We conduct a comparative evaluation of FMs, analyzing PEFT, LP, and FFT strategies to determine which approaches and architectures achieve the best trade-off between computational cost and predictive performance.

- **Few-Shot Learning in Prognostic Modeling.** We provide a systematic analysis of FSL performance in clinical prognosis tasks, evaluating how well PEFT methods and FMs generalize under extreme data scarcity. This analysis simulates scenarios common in rare diseases, emerging outbreaks, and underrepresented patient populations.

By answering these questions, we aim to establish a methodological foundation for adapting FMs to clinical prognosis prediction, offering practical insights for deploying robust, efficient, and generalizable AI systems in real-world medical settings. We organized this work as follows: in Section 2, we review prior research on FMs and PEFT within medical imaging, emphasizing the current gap in studies focused on prognostic tasks. In Section 3 we introduce the benchmark datasets and our methodological framework, detailing the model selection based on pretraining paradigms, fine-tuning strategies and the experimental setup. Finally, Section 4 reports the results and corresponding discussion, structured around the three central research questions outlined earlier.

## 2. Related Works

To contextualize our benchmark, we review recent developments in two key areas: the application of FMs in medical imaging and the emergence of PEFT as a practical strategy for adapting these models to medical domain tasks.

### 2.1. Foundation Models in Medical Imaging.

FMs have become a transformative paradigm in AI, driven by large-scale SSL across multiple domains, including medical imaging [26]. Trained on extensive datasets, these models offer general-purpose representations that can be adapted to diverse downstream tasks. However, medical images differ significantly from natural images in semantics, structure, and statistical properties [24], requiring tailored pretraining and adaptation strategies for effective deployment in clinical settings. Within medical imaging, FMs’ development has primarily focused on vision-language models that leverage paired image-text supervision. CLIP [21], trained on 400M web-sourced pairs, inspired several medical adaptations. MedCLIP [39] decouples image-text learning using semantic similarity losses to overcome clinical data limitations. BioMed-CLIP [40], trained on 15M biomedical image-text pairs, extends this idea

across imaging modalities, enabling more robust medical visual-language representations. Specifically for CXRs, several recent models aim to support interpretation and downstream prediction tasks. CheXagent [41], trained on a curated set of 28 public CXR datasets, combines a clinical LLM with a vision encoder to enable multi-task performance and fairness evaluation across demographic groups. DiCoM [42] introduces a novel SSL strategy for CXRs using a student-teacher framework to capture diverse visual concepts beyond single-label supervision, improving generalization and transfer. ELIXR [43] trains a lightweight adapter to align a CXR image encoder with a fixed LLM (PaLM 2 [44]), enabling tasks such as zero-shot classification, semantic search, VQA, and report quality assurance.

In 3D radiography, medical FMs have emerged to model more complex anatomical and temporal structures. Time-to-event pretraining [45] integrates longitudinal EHR data with 3D CT imaging to improve clinical risk prediction, capturing progression signals often missed by static image models. CT-FM [46], trained in contrastive learning on 148,000 CT scan and report pairs, achieves state-of-the-art performance across triage, segmentation, retrieval, and semantic tasks, while demonstrating interpretability and test-retest robustness. In segmentation, general-domain FMs like SAM [47] have been extended to the medical domain via MedSAM [48], a ViT-based model trained on over 1.5M medical image-text pairs. MedSAM outperforms classical architectures on various segmentation tasks, demonstrating the potential of adapting large vision-language FMs to clinical workflows. Despite these advances, the application of FMs to prognosis prediction remains limited. While models such as TITAN [49] and BEPH [50] show potential in survival prediction using histopathology, few FMs explicitly address prognosis from radiological imaging. Integrating temporally structured, multimodal clinical data with image-based representations in settings characterized by data scarcity and class imbalance remains an open challenge. In summary, while domain-specific FMs are advancing automated interpretation and general clinical AI, their adaptation to small-scale, out-of-domain prognosis tasks is still underexplored. Closing this gap requires further research into effective fine-tuning strategies, multimodal fusion, and benchmarking under realistic clinical constraints.

## *2.2. Parameter-Efficient Fine-Tuning in Medical Imaging.*

PEFT has emerged as a practical alternative to full fine-tuning, enabling the adaptation of large-scale pretrained models to downstream tasks by up-

dating only a small subset of parameters [51, 52, 29, 30]. By keeping the majority of the model weights frozen, PEFT strategies significantly reduce computational and memory requirements, making them particularly well-suited for resource-constrained or data-scarce settings commonly encountered in medical imaging. Broadly, PEFT methods can be categorized into three groups [30]: **addition-based** approaches, which inject lightweight trainable components into the network (e.g., adapters, prompt tuning); **specification-based** methods, which restrict updates to specific parameters such as biases, as in BitFit [31]; and **reparameterization-based** strategies, such as LoRA [32], which fine-tune the model in a low-rank subspace. Variants like QLoRA [35] and VeRA [53] further enhance efficiency through quantization or fixed random projections with learnable scaling. In medical imaging, PEFT has gained attention as a means to extend the capabilities of FMs to diagnostic imaging data [54, 55]. While most research to date has concentrated on diagnostic classification, there is growing interest in expanding PEFT to more complex settings, such as prognosis. For instance, FairMedFM [55] bench-marked 20 FMs across 17 datasets, uncovering performance disparities among demographic groups, while FairTune [54] proposed a PEFT parameter selection scheme optimizing both fairness and accuracy. Complementing this, Dutt et al. [51] conducted a comprehensive evaluation of 17 PEFT strategies on CNN and transformer architectures, showing marked improvements in low-data conditions. Beyond classification, PEFT has also been employed in segmentation tasks. For example, Med-SA [56] adapted SAM [47] with domain-specific modules, and MedSAM-U [57] introduced uncertainty-aware prompt tuning for better segmentation precision. In multimodal contexts, PEFT facilitates cross-modality transfer: PEMMA [58] applied LoRA to adapt CT models to PET segmentation with minimal trainable parameters, while PeFoMed [59] demonstrated the adaptability of large vision-language models to visual question answering and report generation. PEFT methods have been applied in the clinical context to adapt large pretrained language models for clinical tasks with reduced computational demands. Gema et al. [60] introduced a two-step PEFT framework, combining specialized adapter layers for domain adaptation and downstream tasks, which improved performance across various clinical outcome prediction datasets. Moreover, FSL has emerged as a promising training paradigm that enables models to generalize from only a handful of labeled examples [36]. Specifically, Few-shot classification is a central task within FSL, and involves recognizing unseen classes given only a few labeled instances after the pretraining phase [37].

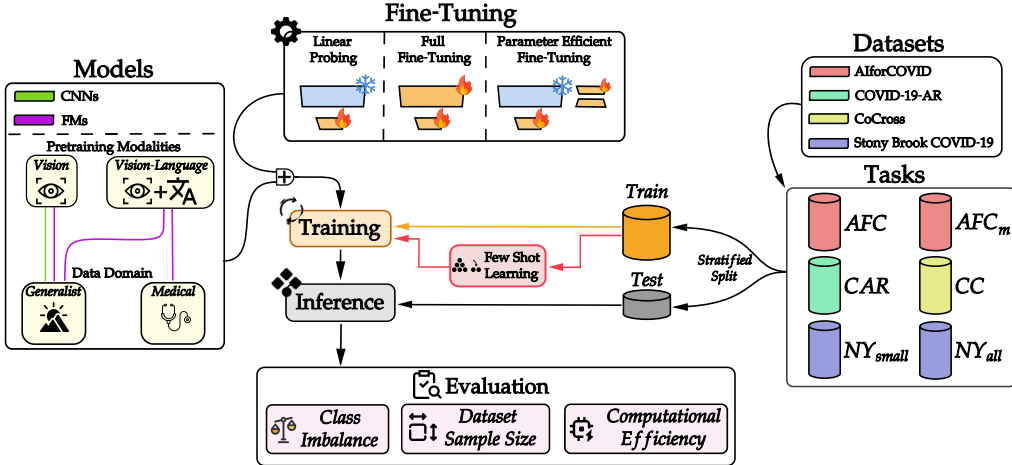


Figure 1: Overview of the methodological framework. The pipeline is structured into five main stages: dataset, models, fine-tuning, training (w/ or w/o FSL) and inference/evaluation.

Recent findings suggest that fine-tuning pretrained ViT directly on new test classes yields competitive performance in FSC [61]. However, such fine-tuning remains computationally expensive and prone to overfitting in low-data regimes typical of medical imaging. Some of these techniques employ PEFT [38], in order to dramatically reduces computational and memory costs, enabling the adoption of these large models in data- and resource-constrained clinical environments. Lastly, Chen et al. [62] demonstrates the potential of large language models for clinical prognosis prediction under few-shot learning conditions. Focusing on immunotherapy outcomes, the authors’ findings highlight the relevance of pretrained language models for rare disease prediction and reinforce the growing role of efficient adaptation techniques in clinical applications.

Despite growing interest in applying PEFT in medical and FSC tasks, not many works has addressed its use in prognostic modeling, especially under clinically realistic constraints such as severe class imbalance or sample size, that is critical for enabling scalable, real-world deployment of FMs in real clinical settings.

### 3. Materials & Methods

Our experimental pipeline, illustrated in Fig. 1, defines the key methodological framework adopted in this benchmark. It is structured into five main stages, ensuring a systematic and reproducible evaluation of fine-tuning strategies and model transferability for clinical prognosis prediction using medical imaging data. Each stage has been carefully designed to simulate real-world clinical conditions, balancing methodological rigor with practical applicability.

**Dataset Selection.** We employ four publicly available COVID-19 CXR datasets annotated with a variety of prognostic outcomes, including mortality, severity, and ICU admission. These datasets were selected to cover a wide range of clinical scenarios and data challenges, including varying degrees of class imbalance, outcome heterogeneity, and differences in sample size—ranging from highly underrepresented cases to larger, more balanced datasets. This diversity reflects the complexities typically encountered in real-world prognosis modeling and enables a robust evaluation of model adaptability under different data regimes [63, 64]. Further details of the datasets are provided in Section 3.1.

**Model Categorization.** We systematically evaluate models grouped into two main architectural families. The first includes standard CNNs pretrained on ImageNet using supervised learning, representing strong baselines in medical imaging due to their inductive biases and efficiency in low-data scenarios. The second architectural category, *FMs*), is composed by models pretrained through self-supervised or contrastive learning, either on large-scale general image-text datasets or specialized medical datasets. This categorization enables us to explore the interplay between architectural design, pretraining paradigms, and domain specificity in prognosis prediction tasks.

**Fine-Tuning Strategies.** Each model undergoes adaptation to the target prognostic tasks using one of several fine-tuning strategies. These include FFT as a performance upper bound, LP to evaluate the quality of frozen representations, and multiple PEFT techniques, which are designed to minimize computational overhead and improve adaptation efficiency. The full range of supported configurations and their applicability to specific architectures are detailed in Section 3.

**Training Regimes.** To assess the generalization capabilities of models under realistic constraints, we benchmark each configuration under two training regimes. In the full-data regime, models are trained using all available labeled samples. In contrast, the FSL regime limits training to as few as 2, 4, 8, or 16 samples per class, simulating extreme data scarcity common in rare disease contexts or emerging health crises. This dual evaluation framework enables a comprehensive analysis of model robustness and the effectiveness of fine-tuning strategies across a spectrum of data availability scenarios.

**Inference & Evaluation.** We evaluate model performance primarily using the Matthews Correlation Coefficient (MCC), a metric known for its robustness in the presence of class imbalance, which is a prevalent issue in prognostic datasets. This ensures a fair assessment of model predictions across both majority and minority classes. An Additional evaluation metric, Area Under the Precision-Recall Curve (AUPRC), is employed to provide a more complete understanding of the model behavior.

This framework establishes a rigorous foundation for the analyses presented in the following sections, where we discuss in detail the datasets employed, the models and fine-tuning strategies evaluated, and the experimental design used to systematically address the research questions of this study.

### 3.1. Datasets

In this work, we evaluate four publicly available COVID-19 chest X-ray (CXR) datasets selected for their relevance to prognosis prediction and their diversity in task definition, class imbalance, and sample size. Focusing on a common pathological context allows us to benchmark out selected set of model under consistent disease representation while capturing real-world challenges such as extreme data scarcity, heterogeneous imaging frequency, and clinical outcome variability.

Each dataset is annotated with different prognostic task, from mortality, severity, to ICU admission, and collectively spans balanced to highly imbalanced distributions and small to large sample sizes. Standardized care protocols during the pandemic ensure outcome consistency across datasets, enabling reliable comparisons [63, 64].

Table 1 reports the main statistics, including image count, patient numbers, and class distributions.

Dataset	Task	Labels	#N	#P	#C
AIforCOVID [65]	Severity Outcome ( <b>AFC</b> )	Mild: 839 Severe: 746	1585	1585	6
	Mortality ( <b>AFC<sub>m</sub></b> )	Alive: 1336 Deceased: 249	1585	1585	6
COVID-19-AR [66]	ICU Admission ( <b>CAR</b> )	Yes: 28 No: 71	99	99	1
CoCross [67]	ICU Outcome ( <b>CC</b> )	Alive: 243 Deceased: 146	389	150	1
Stony Brook COVID-19 [68]	Mortality ( <b>NY<sub>small</sub></b> )	Alive: 1183 Deceased: 182	1365	1365	1
	Mortality ( <b>NY<sub>all</sub></b> )	Alive: 8742 Deceased: 4897	13639	1365	1

Table 1: Detailed overview for the COVID-19 CXR datasets used in this benchmark, among with each prognosis prediction task. **#N**: total number of samples, **#P**: patients, **#C**: medical centers

The **AIforCOVID** dataset [65] comprises 1,585 patients from six Italian hospitals, with two tasks: severity (**AFC**), showing a balanced class distribution (53–47%), and mortality (**AFC<sub>m</sub>**), which is notably imbalanced (85–15%). Both tasks use the same patient cohort and CXRs.

The **CoCross** dataset [67] includes 387 CXRs from ICU patients monitored over time, with a binary ICU outcome label (**CC**) that is moderately imbalanced (63–37%). The **COVID-19-AR** dataset [66], while limited to 99 CXRs, focuses on rural and underrepresented populations. Its ICU admission label (**CAR**) presents a strong imbalance (71–29%), making it a valuable case for evaluating models in extreme low-data regimes.

Lastly, the **Stony Brook COVID-19** dataset [68] is used for mortality prediction with two versions: **NY<sub>small</sub>**, comprising one CXR per patient closest to admission (1,365 CXRs, 87–13% imbalance), and **NY<sub>all</sub>**, containing all CXRs recorded during hospitalization (13,639 images, 64–36% imbalance). Both versions share the same patient population, allowing controlled comparisons of dataset size and class imbalance effects on prognostic modeling.

The selected datasets provide a suitable ground for prognostic assessment, incorporating key aspects frequently observed in prognosis tasks, such as high task complexity, variability in sample sizes, and different degrees of

Model	Pretraining	Data	Vision Backbone	#Params (M)	Embed Dim	Category
ResNet18 [69]	Supervised	ImageNet [14]	ResNet18	11.7	-	CNNs
ResNet50 [69]	Supervised	ImageNet [14]	ResNet50	23.5	-	CNNs
DenseNet121 [70]	Supervised	ImageNet [14]	DenseNet121	7.9	-	CNNs
DINOv2 <sub>s</sub> [71]	Self-supervised	LVD-142M [71]	ViT-S/14	21	384	FMs
DINOv2 <sub>b</sub> [71]	Self-supervised	LVD-142M [71]	ViT-B/14	86	512	FMs
DINOv2 <sub>l</sub> [71]	Self-supervised	LVD-142M [71]	ViT-L/14	300	768	FMs
CLIP-Large [21]	Contrastive	LAION-400M [72]	ViT-L/14	300	768	FMs
MedCLIP <sub>c</sub> [39]	Contrastive	CheXpert <sup>†</sup> + MIMIC <sup>†</sup> [73, 41]	ResNet50	23	-	FMs
MedCLIP <sub>v</sub> [39]	Contrastive	CheXpert <sup>†</sup> + MIMIC <sup>†</sup> [73, 41]	Swin-T	27	-	FMs
PubMedCLIP [74]	Contrastive	ROCO <sup>†</sup> [75]	ViT-B/14	86	512	FMs
BioMedCLIP [40]	Contrastive	PMC-15M <sup>†</sup> [40]	ViT-B/14	86	512	FMs

Table 2: Summary of the selected models, detailing their architectural category, pretraining strategy, pretraining dataset (with  $\dagger$  indicating medical data), vision backbone type, number of vision encoder parameters (in millions), and embedding dimension.

class imbalance. The influence of these prognostic data characteristics will be systematically analyzed and discussed in relation to the performance achieved by the various FMs across the different tasks, with the corresponding results presented in Section 4.

### 3.2. Models

For this study, we include a diverse set of models that have been pre-trained using three distinct learning paradigms: *supervised pretraining*, *self-supervised pretraining*, and *contrastive language-image pretraining*. This design supports a controlled comparison of how architectural choices and pre-training strategies affect the transfer to prognosis tasks. A summary of the included models is provided in Table 2, alongside with further details about architectural class, pretraining strategy, pretraining dataset, vision backbone type, number of vision encoder parameters and embedding dimension, where the symbol “–” in the embedding dimension column indicates that the model is not Transformer-based or does not have a uniform embedding size.

We include both **ResNet18** and **ResNet50** as representative CNN architectures due to their established success in transfer learning for medical imaging, particularly when pretrained on natural image datasets like ImageNet [15, 16]. Their low parameter count, strong inductive biases, and efficient training dynamics make them particularly effective in low-data settings, where overfitting and computational constraints are critical concerns. For the self-supervised learning (SSL) paradigm, we adopt **DINOv2** [71], a state-of-the-art vision transformer (ViT)-based model that has shown competitive performance in medical imaging tasks [76, 55]. Its ability to extract rich,

transferable features from unlabeled data makes it highly suitable for prognostic tasks in resource-constrained environments, where annotated datasets are often scarce. We include **CLIP-Large** [21] to assess the transferability of general-purpose contrastive language-image pretraining in prognosis prediction. Moreover, given the widespread adoption of contrastive pretraining also in the medical applications, we evaluate three medical pretrained variants: **MedCLIP** [39], **PubMedCLIP** [74], and **BioMedCLIP** [40] all pretrained on large-scale multimodal biomedical datasets. These models offer an ideal test ground to analyze domain-specific pretraining on our prognosis downstream tasks. For these multimodal architectures, we utilize only the vision encoder, integrating it with a task-specific linear adapter layer designed for each prognostic prediction task. This diverse selection, spanning architectural types, pretraining strategies, and domain alignments, enables a systematic evaluation of adaptation strategies and model robustness in extreme low-data prognostic settings.

### 3.3. PEFT, Linear Probing and Full Fine-Tuning

Family	FT Model	LoRA	VeRA	IA <sup>3</sup>	BitFit	LP	FFT
CNNs	ResNet18	✓			✓	✓	✓
	ResNet50	✓			✓	✓	✓
	DenseNet121	✓			✓	✓	✓
FMs	DINOv2 <sub>s,b,l</sub>	✓	✓	✓	✓	✓	✓
	CLIP-Large	✓	✓	✓	✓	✓	✓
	MedCLIP <sub>c</sub>	✓			✓	✓	✓
	MedCLIP <sub>v</sub>	✓		✓	✓	✓	✓
	PubMedCLIP	✓	✓	✓	✓	✓	✓
BioMedCLIP	BioMedCLIP	✓	✓	✓	✓	✓	✓

Table 3: Overview of model architectures and their compatible PEFT strategies. ✓ indicates the PEFT method is applicable to the corresponding model.

In the context of medical imaging prognosis, adapting deep learning models to clinical outcome prediction remains a challenging task that requires balancing computational efficiency with effective knowledge transfer. Given the characteristics of our datasets—limited sample size and class imbalance—we evaluate several PEFT techniques against standard LP and FFT, applied

across models pretrained with diverse learning paradigms and datasets (Section 3.2). Table 3 summarizes the compatibility of each PEFT method with the considered architectures.

**Low-Rank Adaptation (LoRA)** [32] introduces trainable low-rank matrices while keeping the pretrained weights frozen. By decomposing weight updates into two smaller matrices, it significantly reduces the number of trainable parameters while preserving the performance of the original model. This is particularly beneficial in prognosis tasks, where data scarcity makes overfitting a risk. Although commonly applied to transformers [77, 29], we also extend its evaluation to CNNs to assess its versatility across architectural types.

**Vector-based Random Matrix Adaptation (VeRA)** [53] builds upon LoRA by employing fixed random projections shared across layers, modulated by trainable scaling vectors. This further reduces the parameter footprint while retaining competitive performance. Due to its reliance on a uniform feature space, VeRA is only applied to ViT-based models, excluding CNNs and the hierarchical Swin-based MedCLIP<sub>v</sub>.

**BitFit** [31] is a sparse fine-tuning method that updates only the bias terms of the model. Despite modifying fewer than 0.1% of the parameters, it often yields strong results, making it particularly attractive for prognosis applications where training resources and data availability are limited. Moreover, it offers insights into how far inductive biases encoded in pretrained models can be selectively activated through minimal adaptation.

**Infused Adapter by Inhibiting and Amplifying Inner Activations (IA<sup>3</sup>)** [33] adapts a pretrained model by inserting multiplicative gates that modulate intermediate activations. These scaling vectors act on attention and feed-forward layers without altering the model’s main parameters. Initialized to preserve the model’s original behavior, IA<sup>3</sup> enables stable and efficient adaptation, especially effective in low-data scenarios typical of prognosis tasks.

In addition to PEFT, we include **FFT** and **LP** as reference fine-tuning settings. FFT updates all parameters and serves as the upper-bound useful to evaluate the full model adaptability to new downstream tasks, while LP freezes the backbone and optimizes only a linear classification head, offering a lower-bound that evaluates the quality of pretrained features [21, 78]. Using both benchmarks establishes a performance spectrum, within which we assess the efficiency and expressiveness of PEFT strategies in real-world clinical settings.

### 3.4. Few-Shot Learning Analysis

FSL refers the problem setting in which a model must learn to generalize from only a few labeled examples per class [79]. This paradigm is particularly relevant in medical imaging, where annotated data is often scarce due to high labeling costs and limited expert availability. To evaluate the robustness and adaptability of PEFT methods under such constraints, we design a systematic few-shot learning benchmark. Let  $\mathcal{Y} = \{1, \dots, C\}$  denote the set of class labels. For a fixed number of shots  $k$ , the few-shot training set is defined as follows:

$$\mathcal{D}_{\text{train}}^{(k)} = \{(x_i, y_i) \mid y_i \in \mathcal{Y}, 1 \leq i \leq kC\} \quad (1)$$

where exactly  $k \in \mathbb{N}$ , represents the samples drawn for each class, leading to a total of  $kC$  training examples per experiment. We evaluate all PEFT strategies listed in Table 3, excluding FFT due to its tendency to overfit in low-data regimes. The training protocol follows a geometric progression over the number of shots:  $k \in \{2, 4, 8, 16, 32\}$ . This allows us to systematically characterize the scaling behavior of each method as the number of labeled samples increases. By exploring this setup, we aim to determine the extent to which PEFT approaches can effectively adapt to prognosis prediction tasks with extremely limited data, providing insights into their feasibility for real-world medical applications where annotated data could be extremely scarce.

### 3.5. Experimental Setup

In this section, we detail the experimental setup used to evaluate all models, covering training configurations, loss functions, evaluation metrics, and architectural considerations.

All experiments followed a uniform configuration for the fine-tuning. Optimization was performed using Stochastic Gradient Descent (SGD) with a momentum of 0.9, weight decay of  $10^{-4}$ , and an initial learning rate of  $10^{-3}$ . Training proceeded for a maximum of 1000 epochs, with a 50-epoch warm-up phase, and employed early stopping with a patience of 50 epochs to mitigate overfitting. We used a batch size of 128 for larger tasks (AFC,  $\text{AFC}_m$ , NY<sub>small</sub>, and NY<sub>all</sub>), and 32 for smaller datasets (CAR, CC) to match their lower dimensionality.

For model validation, we opted for a 5-fold cross-validation for all datasets, with the exception of the multi-centric AFC and  $\text{AFC}_m$  datasets. In these cases, we employed Leave-One-Center-Out (LOCO) validation, which better

reflects real-world deployment scenarios by accounting for inter-center variability, a critical factor in multi-institutional medical imaging studies. For the low-rank adaptation methods (LoRA and VeRA), we systematically varied the rank parameter  $r \in \{4, 8, 16\}$  to balance efficiency and expressiveness. Lower ranks reduce the number of trainable parameters, while higher ranks allow more task-specific adaptation.

This variation helps assess the sensitivity of each method respect dimensionality of the adaptation space and how it is impacting the adaptation on the downstream tasks performance. All models employed in this study were equipped with a task-specific classification head, appended to the output of the vision backbone. Feature representations were extracted from the final block of each model and passed through a lightweight linear layer to produce the final logits. In the case of Vision Transformer (ViT) and foundation model (FM) architectures, we consistently used the class token as the global feature descriptor. This design choice ensures structural and dimensional homogeneity across all architectures, facilitating fair comparisons across PEFT strategies and model types.

Due to the high class imbalance and limited data, a class-weighted Binary Cross-Entropy loss was computed on top of each classification head to ensure robustness across all the tasks. The loss is defined as:

$$\mathcal{L}_{BCE} = -\frac{1}{N} \sum_{i=1}^N w_i [y_i \log(\hat{y}_i) + (1 - y_i) \log(1 - \hat{y}_i)], \quad (2)$$

where  $w_i$  denotes the inverse class-frequency weight for sample  $i$ , and  $\hat{y}_i$  is the predicted probability. The loss function in Eq. 2 was applied uniformly across all experimental settings, including every architectural variant, fine-tuning strategy, and FSL scenarios. This ensures consistency and comparability in training dynamics and evaluation.

Regarding evaluation metrics, we adopted the Matthews Correlation Coefficient (MCC) as our primary metric due to its robustness in extreme class imbalance conditions [80]. The metric ranges from -1 to 1, where 1 indicates perfect prediction, 0 corresponds to random guessing, and -1 denotes total disagreement between predictions and ground truth. Indeed, it considers true and false positives and negatives simultaneously, being well-suited for prognosis tasks where the minority class is typically of greater clinical interest yet severely underrepresented in the data (e.g., progression or adverse outcome). To complement MCC, we also report the Precision-Recall Area Under the

Curve (PR-AUC), which is more sensitive than ROC-AUC to the performance on the positive (minority) class and is thus better aligned with the requirements of our benchmark’s tasks [81]. From the hardware perspective, all experiments were conducted using the PyTorch framework on a cluster equipped with 10 NVIDIA TESLA A40 GPUs. The complete code-base is publicly available at [https://github.com/fruffini/PEFT\\_Prognosis](https://github.com/fruffini/PEFT_Prognosis).

## 4. Results and Discussion

In this section, we highlight the representative observations and outcomes obtained in the benchmark, obtained from fine-tuning the models on our set of datasets on COVID-19 prognosis tasks (both presented in Section 3.2). All the results shown in the following sections are reported using the MCC score, which serves as evaluation metric for the results’ analysis. A complete summary of all results is provided in Table A.4 and Table A.5 for the MCC and *PR-AUC*, where also standard deviations and the first and second best performing technique-model pairs are shown for each dataset. In this section, we present the findings emerging from benchmarking the models introduced in Section 3.2 on our suite of datasets. In the following discussion, we systematically examine different aspect and criticality raised in the introduction, structuring the analysis in two parts: a **Setup** paragraph, outlining the specific experimental setup (i.e., models and PEFT methods analyzed), followed by a **Results** paragraph, which presents and interprets the results obtained combining models, datasets, and fine-tuning strategies.

### 4.1. *What are the most effective fine-tuning strategies for adapting CNN and FM architectures to prognosis tasks?*

Understanding the effectiveness of fine-tuning strategies across different architectural families, CNNs and FMs, is essential for building deployable and scalable systems in medical imaging prognosis. While CNNs have been widely adopted due to their simplicity and inductive biases, recent advancements in large-scale pretrained vision transformers (e.g., ViT, CLIP, DINO) have positioned FMs as highly competitive alternatives. However, it remains unclear how these architectures respond under constrained regimes typical of prognosis data settings, characterized by strong class imbalance and reduced samples sizes, and whether PEFT can consistently bridge the adaptation gap across architectures. Moreover, we extend our analysis to include extreme

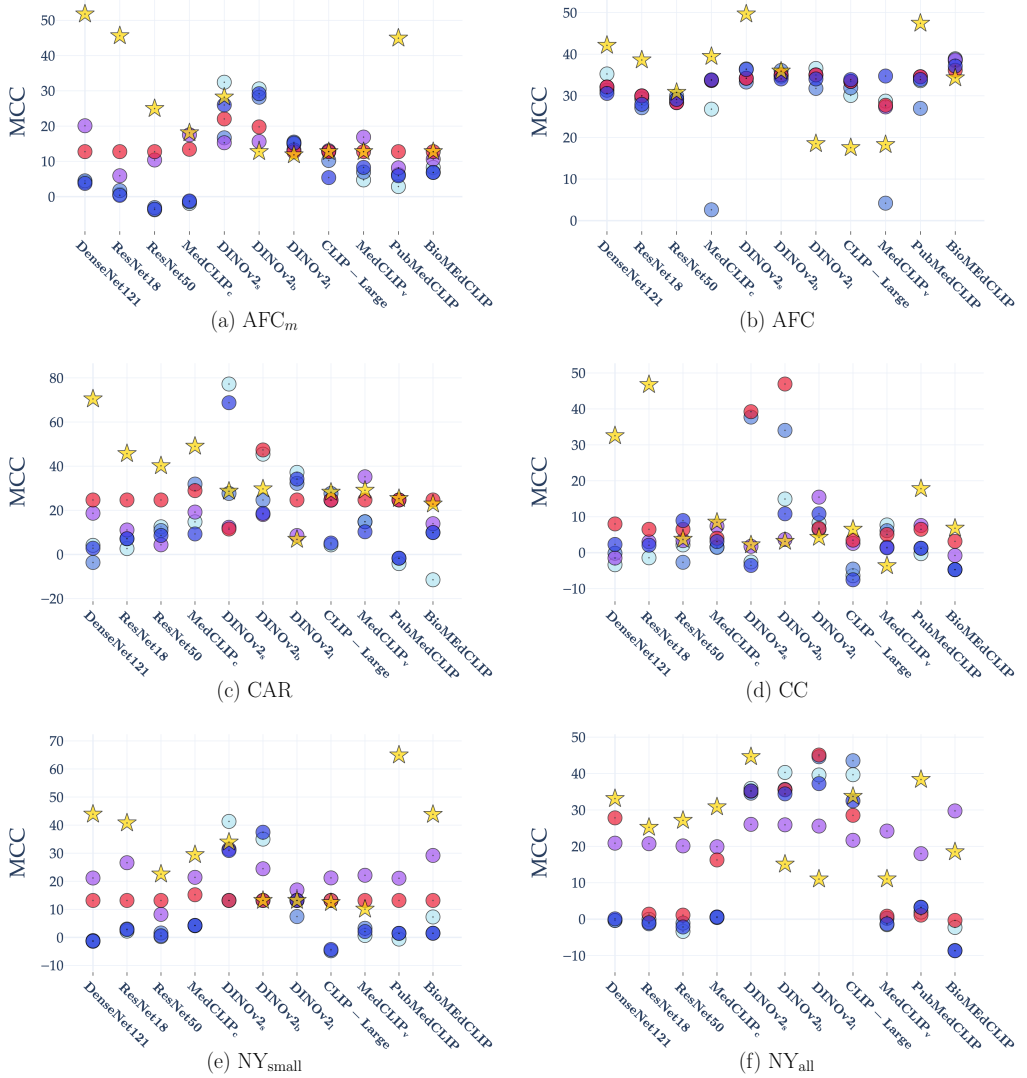


Figure 2: This figure includes only the fine-tuning techniques applicable to both *CNN* and *FM* architecture families. The mean performance over the test set folds for all fine-tuning methods is represented by the  $\circ$  symbol, following the color scheme: **LoRA<sub>r=4</sub>**, **LoRA<sub>r=8</sub>**, **LoRA<sub>r=16</sub>**; **BitFit**, **LP**. The FFT method is uniquely represented by the  $\star$  symbol.

fine-tuning configurations, such as LP and FFT, to further characterize the performance boundaries of minimal versus maximal adaptation strategies.

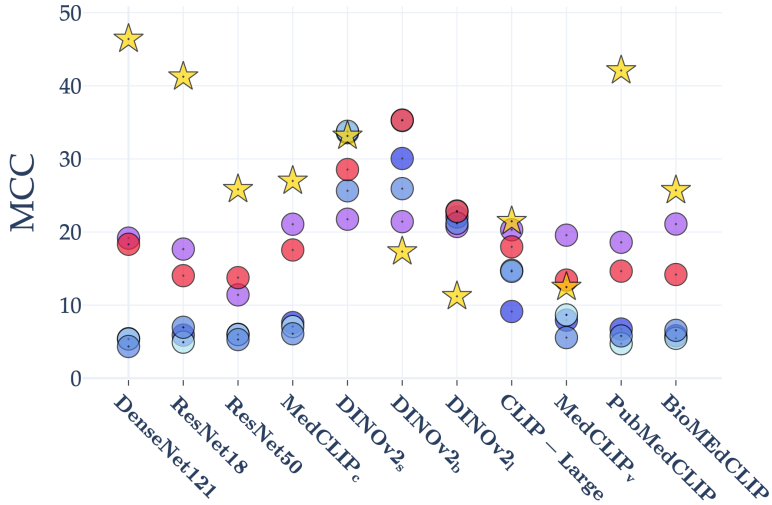


Figure 3: This figure displays the mean over all datasets performances respect only the fine-tuning techniques applicable to both *CNN* and *FM* architecture families. The overall mean for the fine-tuning methods is represented by the  $\odot$  symbol, following the color scheme: **LoRA<sub>r=4</sub>**, **LoRA<sub>r=8</sub>**, **LoRA<sub>r=16</sub>**; **BitFit**, **LP**. The FFT method is uniquely represented by the  $\star$  symbol.

#### 4.1.1. Setup.

We fine-tuned all the models introduced in Section 3.2 on the CXR prognosis tasks described in Section 3.1: to ensure a fair comparison from Table 3 we included only the fine-tuning techniques applicable to both architecture families which are  $\text{AFC}_{mr \in 4,8,16}$ , BitFit, LP, and LP.

#### 4.1.2. Results.

Figure 2 presents the aggregated performance, obtained averaging the results across of the fine tuning techniques by dataset and by model.

We start our analysis with the smallest datasets, CAR and CC (Figures 2.c, 2.d), most PEFT methods fail to yield substantial performance gains under such constrained data conditions, with performance stabilizing around 20% for CAR and 5% for CC. However, certain FT approach combined with models show exceptions to this trend. Notably, BitFit and LoRA yield better results on DINOv2 variants, while FFT consistently outperforms other approaches on CNNs architectures, particularly DenseNet121 and ResNet18 for CC and three CNNs for CAR. These findings indicate that CNNs re-

main more resilient for extremely small datasets, likely due to their lower parameter count and the efficiency conferred by their inductive biases, even if not derived from pretraining the model on medical domain datasets. In contrast, FMs exhibit reduced performance under such conditions, primarily due to their larger parameterization, a limitation further exacerbated by the imbalance that characterize prognosis datasets. Despite this, the promising results achieved with PEFT on the smaller and base DINOv2 variants suggest that, with appropriate fine-tuning strategies, these models can still extract meaningful representations even in extreme low-data regimes. Nonetheless, it is evident that the DINOv2 large fails to generalize in this context—likely due to its higher parameter count, which is disproportionate to the limited dimensionality and scale of the available training data.

A second key insight emerges from comparing AFC and  $\text{AFC}_m$ , two tasks that share the same data samples but differ in balancing conditions. In AFC (Figure 2.a), where the dataset is balanced, PEFT fine-tuning performs consistently across models regardless of the underlying architecture. At the same time DINOv2<sub>s</sub> and PubMedCLIP achieve the best performance, along with CNNs fine-tuned using FFT. This suggests that in scenarios with balanced data, PEFT techniques can successfully leverage pretrained representations without being strongly influenced by model choice [52]. However, in  $\text{AFC}_m$  (Figure 2.b), where class distribution is highly imbalanced, PEFT performance drops significantly, yielding results around 10% in MCC. Interestingly, PEFT methods remain effective only on DINOv2 variants, while FFT consistently outperforms other approaches across all models. These results confirm the strong sensitivity of PEFT techniques to data imbalance, where models struggle to generalize effectively under skewed class distributions.

Lastly, a comparative analysis between  $\text{NY}_{\text{small}}$  and  $\text{NY}_{\text{all}}$  (Figures 2.e, 2.f) highlights dataset size as a critical factor in PEFT effectiveness. In  $\text{NY}_{\text{small}}$ , most PEFT methods fail to achieve meaningful improvements, with only certain DINOv2<sub>s</sub> variants showing moderate success, while FFT on PubMedCLIP emerges as the top performer. In  $\text{NY}_{\text{all}}$ , PEFT techniques exhibit significantly higher performance, in some cases matching or even competing with FFT, particularly on DINOv2 and CLIP-Large. This confirms that PEFT methods require a sufficiently large dataset to effectively adapt and optimize their representations.

In conclusion, our findings further suggest that PEFT methods are highly sensitive to class imbalance and dataset size. Severe imbalance and small sample sizes negatively impact their performance, whereas larger datasets,

even with moderate imbalance, result in significant improvements. DINOv2<sub>s</sub> exhibit an interesting trend in FFT setting: smaller variants tend to outperform larger ones, as seen in Figure 3. This suggests that excessive model complexity may not always translate to better fine-tuning outcomes in low-resource settings. Furthermore, in the comparison between MedCLIP<sub>c</sub> and its supervised pretrained equivalent ResNet50, it is evident that despite MedCLIP<sub>c</sub> was pretrained using SSL, the performance gains are lower than expected. Across most fine-tuning techniques, it achieves only a marginal improvement, with increases of just a few percentage points in the metric score.

Given our demonstration of the consistent benefits provided by PEFT applied to foundation models FMs in medical imaging, we henceforth concentrate our analysis on this paradigm. This decision aligns with established knowledge in the literature, notably Dutt et al. [51], who demonstrated that the advantages of PEFT typically grow with decreasing data volume and increasing model size, particularly benefiting small- to medium-sized datasets common in medical imaging. However, our analysis extends existing understanding by highlighting important limitations: we show that CNN architectures fine-tuned with FFT maintain superior performance in extremely small or severely imbalanced datasets. Conversely, larger-scale FMs often under-perform in these constrained data scenarios. Nevertheless, our novel finding is that specific PEFT strategies can mitigate these challenges for FMs, offering an effective approach to adapt large pretrained models even to particularly demanding tasks such as prognosis.

#### *4.2. Which fine-tuning strategy provides the best trade-off between efficiency and effectiveness when applied to medical prognosis tasks using FMs?*

The design of an effective fine-tuning strategy is a key decision point in adapting large pretrained models to prognosis tasks. Recent advances in FMs have created new opportunities for applying transfer learning in clinical prediction settings. However, the optimal fine-tuning approach remains unclear, particularly in light of growing interest in PEFT strategies. These techniques promise reduced computational and memory costs by updating only a small subset of the model’s parameters, yet their ability to retain performance under medical data constraints is still underexplored. This question is critical in the context of real clinical scenarios.

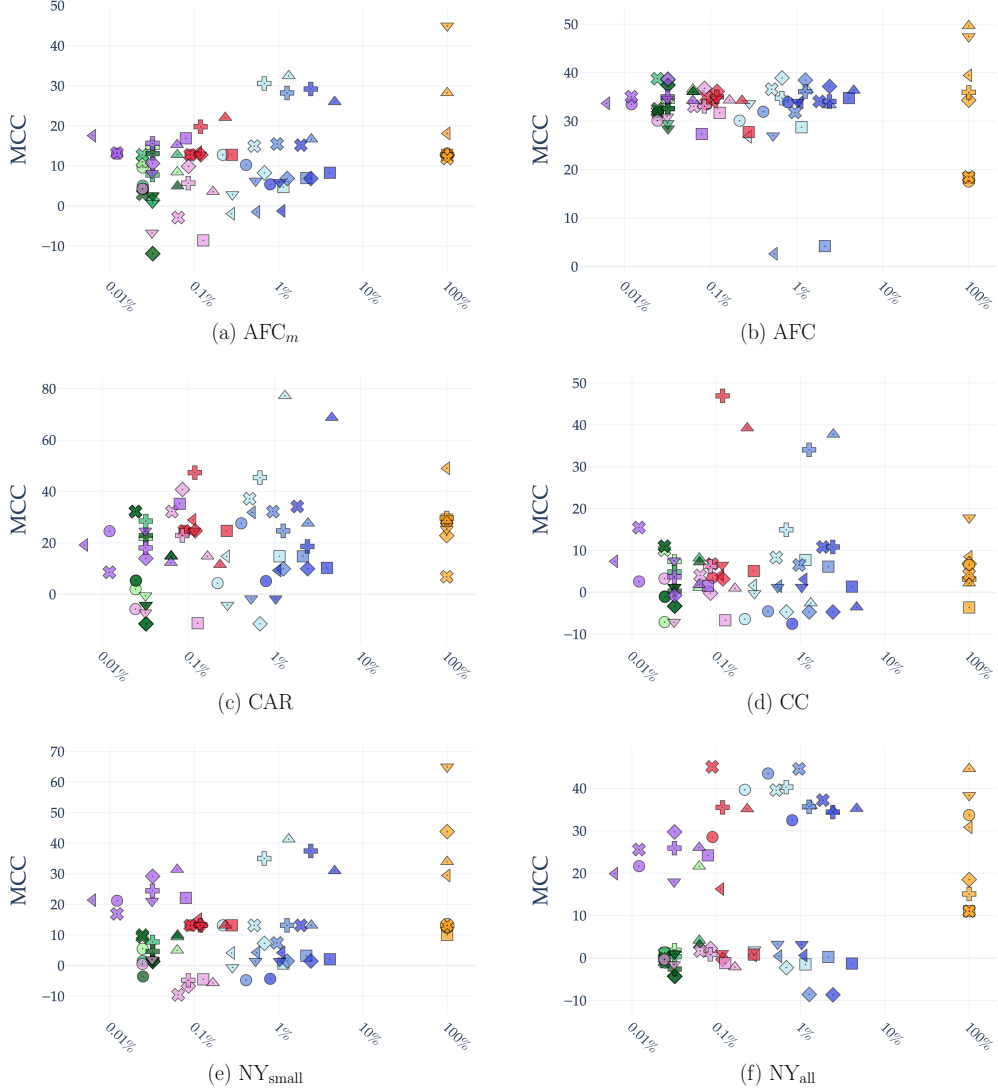


Figure 4: This figure presents one subplot for each dataset, illustrating on the  $y$  axis the MCC results and on the  $x$  axis the percentage of models' parameters trained over the total. Fine tuning techniques and models have a double encoding systems, one based on colors as **LoRA<sub>r=4</sub>**, **LoRA<sub>r=8</sub>**, **LoRA<sub>r=16</sub>**, **VeRA<sub>r=4</sub>**, **VeRA<sub>r=8</sub>**, **VeRA<sub>r=16</sub>**, **BitFit**, **IA<sup>3</sup>**, **LP**, and **FFT**; and one based on the model  $\circ$  (*CLIP-Large*),  $\square$  (*MedCLIP<sub>v</sub>*),  $\diamond$  (*BioMEDCLIP*),  $\oplus$  (*DINOv2<sub>b</sub>*),  $\triangle$  (*DINOv2<sub>s</sub>*),  $\otimes$  (*DINOv2<sub>t</sub>*),  $\triangleleft$  (*MedCLIP<sub>c</sub>*), and  $\triangledown$  (*PubMedCLIP*).

#### 4.2.1. *Setup.*

In this section, we analyze various fine-tuning techniques applied exclusively to FMs, with the combination of PEFT methods and models following Table 3. To maintain consistency, all models were trained using the same experimental settings as discussed in Section 3.5. This analysis aims to provide insights into FMs as a pretraining paradigm, rather than being tied to a specific model architecture. Figure 4 presents the results, where the x-axis represents the percentage of trained FM parameters over the total, and the y-axis indicates the average metric value obtained on the test sets.

#### 4.2.2. *Results.*

We conducted a comprehensive analysis of the results presented in Figure 4, examining performance respect different characteristics of the data, including sample size and class distribution. Furthermore, we evaluated PEFT efficiency by investigating the relationship between model performance and the proportion of the model trainable parameters adapted during fine-tuning. This analysis aimed to quantify the effectiveness of PEFT in relation to their ability to achieve task-specific adaptation while modifying only a small fraction of the original model parameters.

In smaller datasets such as CAR and CC (Figure 4.c, 4.d), most fine-tuning techniques fail to deliver significant improvements, suggesting that despite their parameter efficiency, these methods struggle to adapt and generalize under data constraints. This is particularly evident in Figure 4.d, where most techniques plateau around 10% MCC, with the exception of LoRA<sub>r=8</sub> and BitFit, which perform notably better when applied to DINOv2<sub>l</sub> and DINOv2<sub>s</sub>.

For CAR, results are generally more favorable, with several experiments achieving up to 30% MCC. Notably, LoRA<sub>r=4</sub> and LoRA<sub>r=16</sub> applied to DINOv2<sub>s</sub> reach performance levels close to 80%, indicating that certain configurations can still extract meaningful representations despite limited data. However, in both datasets, FFT consistently underperforms, likely due to the constraints imposed by small sample sizes. These findings suggest that the most parameter-efficient techniques are not always the most effective in low-data scenarios. Factors such as dataset complexity, class imbalance, and the pretraining knowledge of the model play a key role during fine-tuning. Some methods, like LoRA and BitFit, leverage pretrained representations better, while others, such as FFT, struggle due to excessive constraints on the dataset size. This shows that there is no direct correlation between the

percentage of trainable parameters and final performance, indicating that adaptation depends on a combination of model adaptability to capture relevant features discriminant for prognosis tasks.

Another key finding observed is the impact of task imbalance on performance. This analysis is performed comparing AFC and  $\text{AFC}_m$  (Figure 4.a, 4.b, as both datasets contain the same number of samples but differ in class distribution across the two tasks. In the balanced dataset AFC (Figure 4.a), all fine-tuning methods achieve results stable around  $\sim 30\%$  MCC for the majority of the methods, with FFT performing best for DINOv2<sub>s</sub> and PubMedCLIP. However, in the imbalanced task  $\text{AFC}_m$  (Figure 4.b), performance drops significantly despite the dataset size remaining the same. Notably, LoRA and BitFit still manage to reach 35% MCC, indicating resilience to class imbalance. This highlights that dataset properties, beyond size alone, play a crucial role in fine-tuning outcomes. When fine-tuning FMs, class balance must be carefully considered, as intrinsic model biases can lead to misleadingly poor results if not properly accounted for.

A similar pattern emerges when comparing  $\text{NY}_{\text{small}}$  and  $\text{NY}_{\text{all}}$  (Figures 4.e and 4.f), which represent the same task but differ in dataset size by a factor of ten. Several fine-tuning techniques remain around  $\sim 10\%$ , but DINOv2<sub>s</sub> and *DINOv2<sub>b</sub>* achieve the best results with LoRA, BitFit, and FFT on  $\text{NY}_{\text{all}}$ , particularly for DINOv2 and CLIP-Large. In contrast, only LoRA performs well on  $\text{NY}_{\text{small}}$ . Interestingly, FFT achieves the highest performance on  $\text{NY}_{\text{small}}$ , mirroring the behavior observed on  $\text{AFC}_m$ . However, on  $\text{NY}_{\text{all}}$ , its performance aligns with PEFT methods that train fewer parameters, suggesting that the larger dataset improves adaptation, reducing the need for extensive parameter updates needed in FFT. FT effectiveness is strongly influenced by the pretraining model’s inherent biases. In general, FFT achieves the best performance, particularly for PubMedCLIP and DINOv2 variants. This suggests that for efficient adaptation, a generalist model like DINOv2, despite lacking domain-specific medical pretraining, performs best across diverse tasks. In contrast, a biomedical-specific model like PubMedCLIP benefits the most from FFT, emphasizing the importance of selecting fine-tuning strategies based on both model characteristics and dataset properties.

These findings confirm that there is no one-size-fits-all fine-tuning strategy. The optimal choice depends on dataset size, class distribution, and model-specific inductive biases. While FFT remains the gold standard in large, balanced datasets, its limitations become evident in small or skewed conditions. Conversely, PEFT methods like LoRA and BitFit, though parameter-

efficient, are highly sensitive to dataset properties. Given these results, in the following sections we move our attention to the evaluation of PEFT techniques under FSL conditions. These scenarios are particularly relevant in real-world clinical practice, where annotations are limited and new tasks must be adapted quickly with minimal supervision. By isolating PEFT in this extreme regime, we aim to better understand their practical utility and identify configurations that offer robust generalization despite severe training constraints.

#### *4.3. Can PEFT strategies offer robust and generalizable adaptation in Few-Shot Learning scenarios involving FMs, under prognosis data constraints?*

In real-world medical imaging applications, particularly in prognosis prediction, annotated datasets are often extremely limited. As a result, models are frequently required to adapt from only a few training samples per class. This constraint defines FSL setting, a particularly challenging yet clinically realistic scenario. In such contexts, large-scale full fine-tuning is impractical and prone to overfitting, motivating the need for lightweight and efficient adaptation strategies. PEFT techniques have emerged as a promising direction to address these challenges. However, their effectiveness in extreme low-resource regimes, particularly when applied to high-capacity FMs, remains poorly understood. For this reason, in the following sections we discuss the analysis on the performance obtained from FMs on our COVID-19 prognostic datasets.

##### *4.3.1. Setup.*

We also analyzed the efficacy of PEFT in low-resource settings, following the few-shot learning approach described in Section 3.4. All results are averaged across FM architectures, so the final plots represent the overall behavior of each technique on a specific dataset. We included all the datasets listed in Table 1, except for  $NY_{all}$ . Since the task remains the same while the sample size is reduced, we only evaluate performance on  $NY_{small}$ . Given the FSL setting, the number of training samples is identical for both datasets, meaning the additional samples in  $NY_{all}$  do not impact the training phase. Therefore, we focus on  $NY_{small}$  for evaluation, as it provides the most relevant insights under the constrained training conditions. The performance used for evaluation remains consistent with previous experimental setups, as the test sets are the same across validation strategies. The only difference is the training sample size, which is deliberately limited in the FSL setting as described in

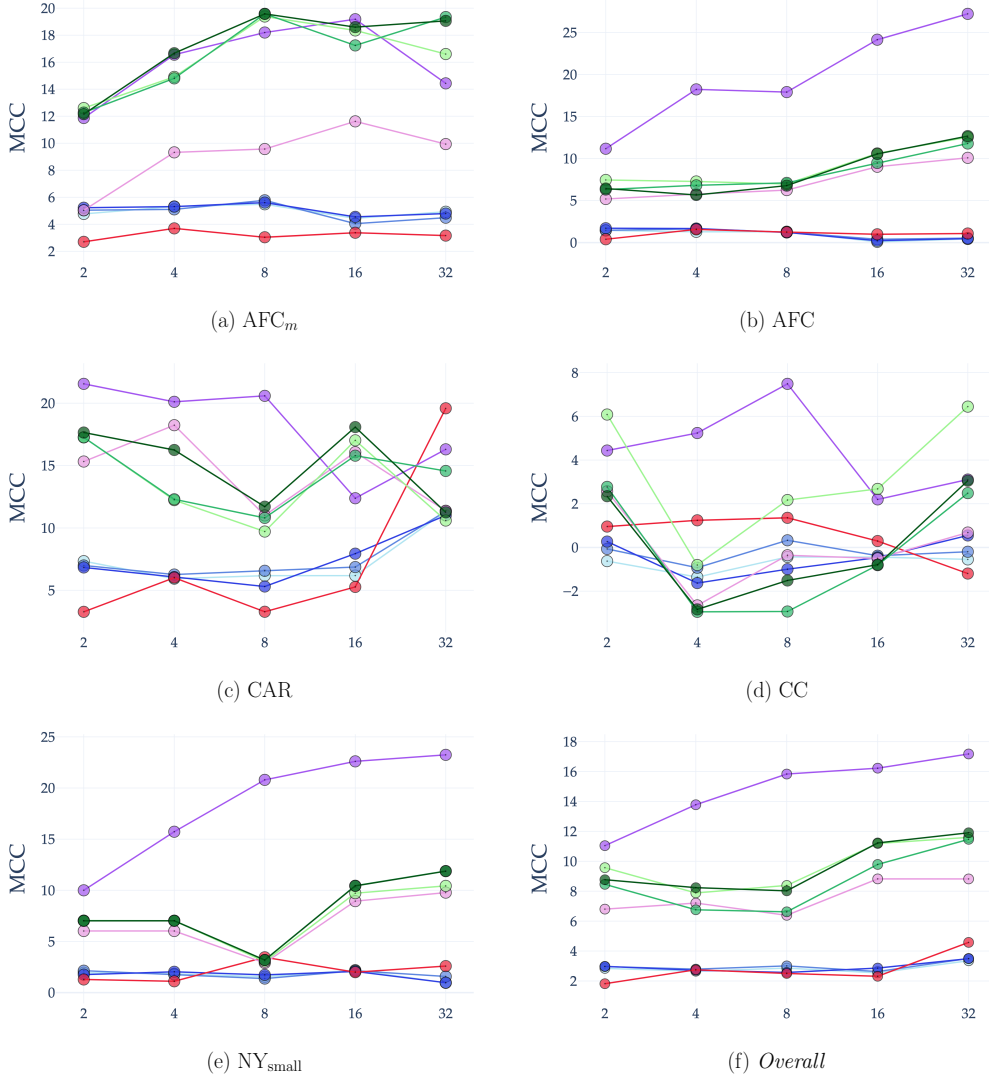


Figure 5: This figure illustrates the average performance of PEFT techniques across different datasets. The x-axis represents the number of shots (examples) per class, while the y-axis reports the corresponding performance metrics. The final subplot provides an aggregated view, displaying the overall average performance of each technique across all datasets for a more comprehensive comparison. PEFT techniques have a single encoding system based on colors: **LoRA<sub>r=4</sub>**, **LoRA<sub>r=8</sub>**, **LoRA<sub>r=16</sub>**, **VeRA<sub>r=4</sub>**, **VeRA<sub>r=8</sub>**, **VeRA<sub>r=16</sub>**, **BitFit**, **IA<sup>3</sup>**, **LP**.

Section 3.4. Figure 5 presents the average performances obtained, where the x-axis represents the number of shots (examples) per class, and the y-axis reports performance metrics. The last subplot also shows the overall average performance of each technique across all datasets, providing a comprehensive overview of the results.

#### 4.3.2. Results.

We analyze the results presented in Figure 5. The first key observation is that, across all datasets, performance remains substantially lower than expected. However, an interesting pattern emerges when comparing the AFC dataset in its balanced and imbalanced versions (Figures 5.a and 5.b). In  $\text{AFC}_m$ , the best results were obtained with VeRA, one of the most parameter-efficient approaches, suggesting that efficiency plays a role in this specific setting. However, the overall performance across all datasets appears highly inconsistent, showing no clear evidence of a robust and repeatable trend. In AFC and  $\text{NY}_{\text{small}}$  (Figure 5.e), LP achieves the best absolute performance, contrasting with the results from AFC, where LP alone performed best. This discrepancy may be linked to the parameter space, as the number of available samples is highly constrained. It is likely that the limited dataset size affects the model’s ability to effectively predict the task. Similar trends were observed in the fine-tuning settings explored in Section 4.2, where most methodologies failed to achieve satisfactory performance. Several factors could contribute to this, including the adaptability of foundation models, the efficacy of fine-tuning methods, or the complexity of the tasks themselves.

Given these observations, we strongly believe that under prognosis-related data settings, achieving robust performance remains challenging. FMs, despite their strong representation capabilities, struggle in FSL settings due to their high parametrization and reliance on large-scale data for effective adaptation. The inherent complexity of prognosis tasks further amplify these challenges, as subtle visual cues correlated with clinical outcomes require a fine balance between feature extraction and model adaptability. The major issue is that achieving a sufficiently generalizable network in FSL settings is highly difficult when the test set maintains the natural class imbalance inherent in the dataset distribution, while the training sets are artificially rebalanced using the geometric progression adopted for this experimental setup (Section 3.4).

Nevertheless, LP demonstrates to be the most promising approach in extreme low-resource conditions (Figure 5.f). Additionally, even with stronger

imbalances, LP performs well when the number of samples is sufficient, as seen in  $NY_{small}$  and  $AFC_m$ . This suggests that, while FMs struggle in highly constrained data regimes, certain fine-tuning strategies can still enable meaningful adaptation.

## 5. Conclusions

In this work, we conducted a comprehensive benchmark to assess the effectiveness of fine-tuning strategies, ranging from FFT and LP to several state-of-the-art PEFT methods, across a diverse set of models, including both CNNs and FMs. Focusing on COVID-19 prognosis tasks derived from publicly available chest X-ray datasets, we systematically explored how different fine-tuning approaches perform under varying data constraints, with particular attention to dataset size, class imbalance, and FSL scenarios.

Our findings lead to several key conclusions:

- **CNNs Remain Strong Baselines in Extreme Low-Data Regimes:** CNNs, particularly when fine-tuned using FFT, consistently outperform FMs on extremely small and highly imbalanced datasets. Their lower parameter count and strong inductive biases make them less prone to overfitting and better suited for clinical scenarios with scarce labeled data.
- **FMs with PEFT Achieve Competitive Performance on Larger Datasets:** while FMs struggle in extreme low-data regimes, they demonstrate superior scalability and adaptability as dataset size increases. PEFT methods like LoRA and BitFit enable effective adaptation of FMs with minimal parameter updates, achieving competitive results with significantly lower computational overhead compared to FFT.
- **PEFT Methods Are Highly Sensitive to Class Imbalance:** across all experiments, the performance of PEFT techniques deteriorates under severe class imbalance, particularly when minority classes represent critical clinical outcomes such as ICU admission or mortality. While FFT remains more robust under these conditions, PEFT methods can still provide substantial gains when dataset balance is moderately improved.

- **Few-Shot Learning Remains Challenging, but Selective PEFT Strategies Offer Promise:** in FSL scenarios, PEFT methods applied to smaller FM variants, such as DINOv2<sub>s</sub>, demonstrate an ability to extract meaningful representations even with extremely limited training data. However, the success of these approaches strongly depends on careful model selection and hyperparameter tuning, highlighting the need for further research on PEFT optimization in clinical few-shot settings.
- **No Universally Optimal Fine-Tuning Strategy:** our benchmark highlights that the effectiveness of a fine-tuning approach depends on the interplay between model architecture, dataset characteristics, and computational constraints. CNNs remain a reliable option for low-resource settings, while FMs paired with appropriate PEFT methods offer scalable and efficient solutions as data availability increases.

Our analysis provides actionable guidelines for selecting fine-tuning strategies in real-world medical prognosis applications. It also underscores the need for continued exploration of PEFT techniques, especially in the context of Few-Shot Learning, to fully unlock the potential of FMs in data-constrained and high-impact clinical environments.

*Limitations..* This study focuses exclusively on COVID-19 chest X-ray prognosis tasks, which, while clinically relevant, may not generalize to other imaging modalities or diseases. Additionally, we rely on publicly available datasets that differ in annotation quality and may not fully capture real-world clinical heterogeneity. Although we evaluated a broad range of models and fine-tuning strategies, the search space remains constrained in terms of PEFT configurations and hyperparameters. Nevertheless, the breadth and standardization of our benchmark enable a consistent and informative assessment of fine-tuning strategies across heterogeneous prognostic tasks, while leaving the exploration of medical prognosis across diverse imaging modalities to future work.

#### 5.0.1. Acknowledgements

Filippo Ruffini is a PhD student enrolled in the National PhD in Artificial Intelligence, XXXVIII cycle, course on Health and life sciences, organized by Università Campus Bio-Medico di Roma. This work was partially supported by: i) the Italian Ministry of Foreign Affairs and International

Cooperation, grant number PGR01156, ii) PNRR MUR project PE0000013-FAIR, iii) PNRR – DM 118/2023. Resources are provided by the National Academic Infrastructure for Supercomputing in Sweden (NAIIS) and the Swedish National Infrastructure for Computing (SNIC) at Alvis @ C3SE, partially funded by the Swedish Research Council through grant agreements no. 2022-06725 and no. 2018-05973.

## References

- [1] D. G. Poalelungi, C. L. Musat, A. Fulga, M. Neagu, A. I. Neagu, A. I. Piraianu, I. Fulga, Advancing patient care: how artificial intelligence is transforming healthcare, *Journal of personalized medicine* 13 (2023) 1214.
- [2] M. Rana, M. Bhushan, Machine learning and deep learning approach for medical image analysis: diagnosis to detection, *Multimedia Tools and Applications* 82 (2023) 26731–26769.
- [3] A. U. Ibrahim, M. Ozsoz, S. Serte, F. Al-Turjman, P. S. Yakoi, Pneumonia classification using deep learning from chest x-ray images during covid-19, *Cognitive computation* 16 (2024) 1589–1601.
- [4] F. Aksu, F. Gelardi, A. Chiti, P. Soda, Toward a multimodal deep learning approach for histological subtype classification in nsclc, in: 2024 IEEE International Conference on Bioinformatics and Biomedicine (BIBM), IEEE, 2024, pp. 6327–6333.
- [5] M. E. H. Chowdhury, T. Rahman, A. A. Khandakar, R. Mazhar, M. A. Kadir, Z. B. Mahbub, K. R. Islam, M. S. Khan, A. Iqbal, N. A. Al-Emadi, M. B. I. Reaz, Can ai help in screening viral and covid-19 pneumonia?, *IEEE Access* 8 (2020) 132665–132676. URL: <https://api.semanticscholar.org/CorpusID:214713518>.
- [6] V. V. Danilov, D. Litmanovich, A. Proutski, A. Kirpich, D. Nefaridze, A. Karpovsky, Y. Gankin, Automatic scoring of covid-19 severity in x-ray imaging based on a novel deep learning workflow, *Scientific reports* 12 (2022) 12791.

- [7] A. Signoroni, M. Savardi, S. Benini, N. Adami, R. Leonardi, P. Gibellini, F. Vaccher, M. Ravanelli, A. Borghesi, R. Maroldi, et al., Bs-net: Learning covid-19 pneumonia severity on a large chest x-ray dataset, *Medical image analysis* 71 (2021) 102046.
- [8] K. Rangarajan, S. Muku, A. K. Garg, P. Gabra, S. H. Shankar, N. Nischal, K. D. Soni, A. S. Bhalla, A. Mohan, P. Tiwari, et al., Artificial intelligence-assisted chest x-ray assessment scheme for covid-19, *European radiology* 31 (2021) 6039–6048.
- [9] C. Buttia, E. Llanaj, H. Raeisi-Dehkordi, L. Kastrati, M. Amiri, R. Meçani, P. E. Taneri, S. A. G. Ochoa, P. F. N. Raguindin, F. Wehrli, F. Khatami, O. P. Espinola, L. Z. Rojas, A. P. de Mortanges, E. F. Macharia-Nimietz, F. Alijla, B. Minder, A. B. Leichtle, N. Lüthi, S. Ehrhard, Y.-A. Que, L. K. Fernandes, W. E. Hautz, T. Muka, Prognostic models in covid-19 infection that predict severity: a systematic review, *European Journal of Epidemiology* 38 (2023) 355 – 372. URL: <https://api.semanticscholar.org/CorpusID:257183054>.
- [10] F. Ruffini, L. Tronchin, Z. Wu, W. Chen, P. Soda, L. Shen, V. Guararsi, Multi-Dataset Multi-Task Learning for COVID-19 Prognosis , in: *proceedings of Medical Image Computing and Computer Assisted Intervention – MICCAI 2024*, volume LNCS 15012, Springer Nature Switzerland, 2024.
- [11] E. S. Adamidi, K. Mitsis, K. S. Nikita, Artificial intelligence in clinical care amidst covid-19 pandemic: a systematic review, *Computational and structural biotechnology journal* 19 (2021) 2833–2850.
- [12] A. G. Gillman, F. Lunardo, J. Prinable, G. Belous, A. Nicolson, H. Min, A. Terhorst, J. A. Dowling, Automated covid-19 diagnosis and prognosis with medical imaging and who is publishing: a systematic review, *Physical and engineering sciences in medicine* (2021) 1–17.
- [13] Y. Zhang, J. Gao, Z. Tan, L. Zhou, K. Ding, M. Zhou, S. Zhang, D. Wang, Data-centric foundation models in computational healthcare: A survey, *arXiv preprint arXiv:2401.02458* (2024).
- [14] J. Deng, W. Dong, R. Socher, L.-J. Li, K. Li, L. Fei-Fei, Imagenet: A large-scale hierarchical image database, in: *2009 IEEE Conference on*

Computer Vision and Pattern Recognition, 2009, pp. 248–255. doi:10.1109/CVPR.2009.5206848.

- [15] A. Ke, W. Ellsworth, O. Banerjee, A. Y. Ng, P. Rajpurkar, CheXTransfer: performance and parameter efficiency of Imagenet models for chest x-ray interpretation, in: Proceedings of the conference on health, inference, and learning, 2021, pp. 116–124.
- [16] M. Raghu, C. Zhang, J. Kleinberg, S. Bengio, Transfusion: Understanding transfer learning for medical imaging, *Advances in neural information processing systems* 32 (2019).
- [17] P. Kora, C. P. Ooi, O. Faust, U. Raghavendra, A. Gudigar, W. Y. Chan, K. Meenakshi, K. Swaraja, P. Plawiak, U. R. Acharya, Transfer learning techniques for medical image analysis: A review, *Biocybernetics and biomedical engineering* 42 (2022) 79–107.
- [18] R. Bommasani, D. A. Hudson, E. Adeli, R. Altman, S. Arora, S. von Arx, M. S. Bernstein, J. Bohg, A. Bosselut, E. Brunskill, et al., On the opportunities and risks of foundation models, *arXiv preprint arXiv:2108.07258* (2021).
- [19] S. Azizi, B. Mustafa, F. Ryan, Z. Beaver, J. von Freyberg, J. Deaton, A. Loh, A. Karthikesalingam, S. Kornblith, T. Chen, V. Natarajan, M. Norouzi, Big self-supervised models advance medical image classification, *2021 IEEE/CVF International Conference on Computer Vision (ICCV)* (2021) 3458–3468. URL: <https://api.semanticscholar.org/CorpusID:231592774>.
- [20] M. Caron, H. Touvron, I. Misra, H. Jégou, J. Mairal, P. Bojanowski, A. Joulin, Emerging properties in self-supervised vision transformers, in: Proceedings of the IEEE/CVF international conference on computer vision, 2021, pp. 9650–9660.
- [21] A. Radford, J. W. Kim, C. Hallacy, A. Ramesh, G. Goh, S. Agarwal, G. Sastry, A. Askell, P. Mishkin, J. Clark, et al., Learning transferable visual models from natural language supervision, in: International conference on machine learning, PMLR, 2021, pp. 8748–8763.

- [22] J. Anton, L. Castelli, M. F. Chan, M. Outters, W. H. Tang, V. Cheung, P. Shukla, R. Walambe, K. Kotecha, How well do self-supervised models transfer to medical imaging?, *Journal of Imaging* 8 (2022) 320.
- [23] D. Wolf, T. Payer, C. S. Lisson, C. G. Lisson, M. Beer, M. Götz, T. Ropinski, Self-supervised pre-training with contrastive and masked autoencoder methods for dealing with small datasets in deep learning for medical imaging, *Scientific Reports* 13 (2023) 20260.
- [24] S. Zhang, D. Metaxas, On the challenges and perspectives of foundation models for medical image analysis, *Medical image analysis* 91 (2024) 102996.
- [25] M. Moor, O. Banerjee, Z. S. H. Abad, H. M. Krumholz, J. Leskovec, E. J. Topol, P. Rajpurkar, Foundation models for generalist medical artificial intelligence, *Nature* 616 (2023) 259–265.
- [26] W. Khan, S. Leem, K. B. See, J. K. Wong, S. Zhang, R. Fang, A comprehensive survey of foundation models in medicine, *IEEE Reviews in Biomedical Engineering* (2025).
- [27] S. Li, L. Lin, Y. Huang, P. Cheng, X. Tang, Text-guided foundation model adaptation for long-tailed medical image classification, in: 2024 IEEE International Symposium on Biomedical Imaging (ISBI), IEEE, 2024, pp. 1–5.
- [28] J.-X. Shi, T. Wei, Z. Zhou, J.-J. Shao, X.-Y. Han, Y.-F. Li, Long-tail learning with foundation model: Heavy fine-tuning hurts, *arXiv preprint arXiv:2309.10019* (2023).
- [29] Z. Han, C. Gao, J. Liu, J. Zhang, S. Q. Zhang, Parameter-efficient fine-tuning for large models: A comprehensive survey, *arXiv preprint arXiv:2403.14608* (2024).
- [30] D. Zhang, T. Feng, L. Xue, Y. Wang, Y. Dong, J. Tang, Parameter-efficient fine-tuning for foundation models, *arXiv preprint arXiv:2501.13787* (2025).
- [31] E. B. Zaken, S. Ravfogel, Y. Goldberg, Bitfit: Simple parameter-efficient fine-tuning for transformer-based masked language-models, *arXiv preprint arXiv:2106.10199* (2021).

- [32] E. J. Hu, Y. Shen, P. Wallis, Z. Allen-Zhu, Y. Li, S. Wang, L. Wang, W. Chen, Lora: Low-rank adaptation of large language models, arXiv preprint arXiv:2106.09685 (2021).
- [33] H. Liu, D. Tam, M. Muqeeth, J. Mohta, T. Huang, M. Bansal, C. A. Raffel, Few-shot parameter-efficient fine-tuning is better and cheaper than in-context learning, *Advances in Neural Information Processing Systems* 35 (2022) 1950–1965.
- [34] C. Lian, H.-Y. Zhou, Y. Yu, L. Wang, Less could be better: Parameter-efficient fine-tuning advances medical vision foundation models, arXiv preprint arXiv:2401.12215 (2024).
- [35] T. Dettmers, A. Pagnoni, A. Holtzman, L. Zettlemoyer, Qlora: Efficient finetuning of quantized llms, *Advances in neural information processing systems* 36 (2023) 10088–10115.
- [36] E. Pachetti, S. Colantonio, A systematic review of few-shot learning in medical imaging, *Artificial intelligence in medicine* (2024) 102949.
- [37] S. Woerner, C. F. Baumgartner, Navigating data scarcity using foundation models: A benchmark of few-shot and zero-shot learning approaches in medical imaging, in: *International Workshop on Foundation Models for General Medical AI*, Springer, 2024, pp. 30–39.
- [38] T. Bansal, S. Alzubi, T. Wang, J. Y. Lee, A. McCallum, Meta-adapters: Parameter efficient few-shot fine-tuning through meta-learning, in: *AutoML*, 2022. URL: <https://api.semanticscholar.org/CorpusID:253840114>.
- [39] Z. Wang, Z. Wu, D. Agarwal, J. Sun, Medclip: Contrastive learning from unpaired medical images and text, in: *Proceedings of the Conference on Empirical Methods in Natural Language Processing. Conference on Empirical Methods in Natural Language Processing*, volume 2022, 2022, p. 3876.
- [40] S. Zhang, Y. Xu, N. Usuyama, H. Xu, J. Bagga, R. Tinn, S. Preston, R. Rao, M. Wei, N. Valluri, et al., Biomedclip: a multimodal biomedical foundation model pretrained from fifteen million scientific image-text pairs, arXiv preprint arXiv:2303.00915 (2023).

- [41] Z. Chen, M. Varma, J.-B. Delbrouck, M. Paschali, L. Blankemeier, D. Van Veen, J. M. J. Valanarasu, A. Youssef, J. P. Cohen, E. P. Reis, et al., Chexagent: Towards a foundation model for chest x-ray interpretation, arXiv preprint arXiv:2401.12208 (2024).
- [42] A. Parida, D. Capellan-Martin, S. Atito, M. Awais, M. J. Ledesma-Carbayo, M. G. Linguraru, S. M. Anwar, Dicom–diverse concept modeling towards enhancing generalizability in chest x-ray studies, arXiv preprint arXiv:2402.15534 (2024).
- [43] S. Xu, L. Yang, C. J. Kelly, M. Sieniek, T. Kohlberger, M. Q. Ma, W.-H. Weng, A. P. Király, S. Kazemzadeh, Z. Melamed, J. Park, P. Strachan, Y. Liu, C. Lau, P. Singh, C. Chen, M. Etemadi, S. R. Kalidindi, Y. Matias, K. Chou, G. S. Corrado, S. Shetty, D. Tse, S. Prabhakara, D. Golden, R. Pilgrim, K. Eswaran, A. Sellergren, Elixr: Towards a general purpose x-ray artificial intelligence system through alignment of large language models and radiology vision encoders, ArXiv abs/2308.01317 (2023). URL: <https://api.semanticscholar.org/CorpusID:260378981>.
- [44] R. Anil, A. M. Dai, O. Firat, M. Johnson, D. Lepikhin, A. Passos, S. Shakeri, E. Taropa, P. Bailey, Z. Chen, et al., Palm 2 technical report, arXiv preprint arXiv:2305.10403 (2023).
- [45] Z. Huo, J. A. Fries, A. Lozano, J. M. J. Valanarasu, E. Steinberg, L. Blankemeier, A. S. Chaudhari, C. Langlotz, N. H. Shah, Time-to-event pretraining for 3d medical imaging, arXiv preprint arXiv:2411.09361 (2024).
- [46] S. Pai, I. Hadzic, D. Bontempi, K. Bressem, B. H. Kann, A. Fedorov, R. H. Mak, H. J. Aerts, Vision foundation models for computed tomography, arXiv preprint arXiv:2501.09001 (2025).
- [47] A. Kirillov, E. Mintun, N. Ravi, H. Mao, C. Rolland, L. Gustafson, T. Xiao, S. Whitehead, A. C. Berg, W.-Y. Lo, et al., Segment anything, in: Proceedings of the IEEE/CVF international conference on computer vision, 2023, pp. 4015–4026.
- [48] J. Ma, Y. He, F. Li, L. Han, C. You, B. Wang, Segment anything in medical images, Nature Communications 15 (2024) 654.

- [49] T. Ding, S. J. Wagner, A. H. Song, R. J. Chen, M. Y. Lu, A. Zhang, A. J. Vaidya, G. Jaume, M. Shaban, A. Kim, et al., Multimodal whole slide foundation model for pathology, arXiv preprint arXiv:2411.19666 (2024).
- [50] Z. Yang, T. Wei, Y. Liang, X. Yuan, R. Gao, Y. Xia, J. Zhou, Y. Zhang, Z. Yu, A foundation model for generalizable cancer diagnosis and survival prediction from histopathological images, *Nature Communications* 16 (2025) 2366.
- [51] R. Dutt, L. Ericsson, P. Sanchez, S. A. Tsaftaris, T. Hospedales, Parameter-efficient fine-tuning for medical image analysis: The missed opportunity, arXiv preprint arXiv:2305.08252 (2023).
- [52] A. Storhaug, J. Li, Parameter-efficient fine-tuning of large language models for unit test generation: An empirical study, arXiv preprint arXiv:2411.02462 (2024).
- [53] D. J. Kopiczko, T. Blankevoort, Y. M. Asano, Vera: Vector-based random matrix adaptation, arXiv preprint arXiv:2310.11454 (2023).
- [54] R. Dutt, O. Bohdal, S. A. Tsaftaris, T. Hospedales, Fairtune: Optimizing parameter efficient fine tuning for fairness in medical image analysis, arXiv preprint arXiv:2310.05055 (2023).
- [55] R. Jin, Z. Xu, Y. Zhong, Q. Yao, D. QI, S. K. Zhou, X. Li, Fairmedfm: fairness benchmarking for medical imaging foundation models, *Advances in Neural Information Processing Systems* 37 (2024) 111318–111357.
- [56] J. Wu, W. Ji, Y. Liu, H. Fu, M. Xu, Y. Xu, Y. Jin, Medical sam adapter: Adapting segment anything model for medical image segmentation, arXiv preprint arXiv:2304.12620 (2023).
- [57] N. Zhou, K. Zou, K. Ren, M. Luo, L. He, M. Wang, Y. Chen, Y. Zhang, H. Chen, H. Fu, Medsam-u: Uncertainty-guided auto multi-prompt adaptation for reliable medsam, arXiv preprint arXiv:2409.00924 (2024).
- [58] N. Saadi, N. Saeed, M. Yaqub, K. Nandakumar, Pemma: Parameter-efficient multi-modal adaptation for medical image segmentation, in: International Conference on Medical Image Computing and Computer-Assisted Intervention, Springer, 2024, pp. 262–271.

- [59] G. Liu, J. He, P. Li, G. He, Z. Chen, S. Zhong, Pefomed: Parameter efficient fine-tuning of multimodal large language models for medical imaging, arXiv preprint arXiv:2401.02797 (2024).
- [60] A. P. Gema, L. Daines, P. Minervini, B. Alex, Parameter-efficient fine-tuning of llama for the clinical domain, in: Clinical Natural Language Processing Workshop, 2023. URL: <https://api.semanticscholar.org/CorpusID:259361061>.
- [61] S. Basu, D. Massiceti, S. X. Hu, S. Feizi, Strong baselines for parameter efficient few-shot fine-tuning, in: AAAI Conference on Artificial Intelligence, 2023. URL: <https://api.semanticscholar.org/CorpusID:257921197>.
- [62] Z. Chen, M. M. Balan, K. Brown, Language models are few-shot learners for prognostic prediction, arXiv preprint arXiv:2302.12692 (2023).
- [63] B. Mamandipoor, R. R. Bruno, B. Wernly, G. Wolff, J. Fjølner, A. Artigas, B. B. Pinto, J. C. Schefold, M. Kelm, M. Beil, et al., Covid-19 machine learning model predicts outcomes in older patients from various european countries, between pandemic waves, and in a cohort of asian, african, and american patients, PLOS digital health 1 (2022) e0000136.
- [64] Z. Jiao, J. W. Choi, K. Halsey, T. M. L. Tran, B. Hsieh, D. Wang, F. Eweje, R. Wang, K. Chang, J. Wu, et al., Prognostication of patients with covid-19 using artificial intelligence based on chest x-rays and clinical data: a retrospective study, The Lancet Digital Health 3 (2021) e286–e294.
- [65] P. Soda, et al., AIforCOVID: Predicting the clinical outcomes in patients with COVID-19 applying AI to chest-X-rays. An Italian multicentre study, Medical image analysis 74 (2021) 102216.
- [66] S. Desai, A. Baghal, T. Wongsurawat, S. Al-Shukri, K. Gates, P. Farmer, M. Rutherford, G. D. Blake, T. Nolan, T. Powell, et al., Chest imaging with clinical and genomic correlates representing a rural covid-19 positive population, (No Title) (2020).
- [67] V. Kilintzis, N. Beredimas, E. Kaimakamis, L. Stefanopoulos, E. Chatzis, E. Jahaj, M. Bitzani, A. Kotanidou, A. K. Katsaggelos,

N. Maglaveras, Cocross: an ict platform enabling monitoring recording and fusion of clinical information chest sounds and imaging of covid-19 icu patients, in: *Healthcare*, volume 10, MDPI, 2022, p. 276.

[68] J. Saltz, M. Saltz, P. Prasanna, R. Moffitt, J. Hajagos, E. Bremer, J. Balsamo, T. Kurc, Stony brook university covid-19 positive cases, (No Title) (2021).

[69] K. He, X. Zhang, S. Ren, J. Sun, Deep residual learning for image recognition, in: *Proceedings of the IEEE conference on computer vision and pattern recognition*, 2016, pp. 770–778.

[70] G. Huang, Z. Liu, L. Van Der Maaten, K. Q. Weinberger, Densely connected convolutional networks, in: *Proceedings of the IEEE conference on computer vision and pattern recognition*, 2017, pp. 4700–4708.

[71] M. Oquab, T. Darcet, T. Moutakanni, H. Vo, M. Szafraniec, V. Khaldov, P. Fernandez, D. Haziza, F. Massa, A. El-Nouby, et al., Dinov2: Learning robust visual features without supervision, *arXiv preprint arXiv:2304.07193* (2023).

[72] C. Schuhmann, R. Vencu, R. Beaumont, R. Kaczmarczyk, C. Mullis, A. Katta, T. Coombes, J. Jitsev, A. Komatsuzaki, Laion-400m: Open dataset of clip-filtered 400 million image-text pairs, *arXiv preprint arXiv:2111.02114* (2021).

[73] A. E. Johnson, L. Bulgarelli, L. Shen, A. Gayles, A. Shammout, S. Horng, T. J. Pollard, S. Hao, B. Moody, B. Gow, et al., Mimic-iv, a freely accessible electronic health record dataset, *Scientific data* 10 (2023) 1.

[74] S. Eslami, C. Meinel, G. de Melo, PubMedCLIP: How much does CLIP benefit visual question answering in the medical domain?, in: A. Vlachos, I. Augenstein (Eds.), *Findings of the Association for Computational Linguistics: EACL 2023*, Association for Computational Linguistics, Dubrovnik, Croatia, 2023, pp. 1181–1193. URL: <https://aclanthology.org/2023.findings-eacl.88/>. doi:10.18653/v1/2023.findings-eacl.88.

[75] J. Rückert, L. Bloch, R. Brüngel, A. Idrissi-Yaghir, H. Schäfer, C. S. Schmidt, S. Koitka, O. Pelka, A. B. Abacha, A. G. Seco de Herrera,

et al., Rocov2: Radiology objects in context version 2, an updated multimodal image dataset, *Scientific Data* 11 (2024) 688.

- [76] Y. Huang, J. Zou, L. Meng, X. Yue, Q. Zhao, J. Li, C. Song, G. Jimenez, S. Li, G. Fu, Comparative analysis of imagenet pre-trained deep learning models and dinov2 in medical imaging classification, in: 2024 IEEE 48th Annual Computers, Software, and Applications Conference (COMP-SAC), IEEE, 2024, pp. 297–305.
- [77] J. He, C. Zhou, X. Ma, T. Berg-Kirkpatrick, G. Neubig, Towards a unified view of parameter-efficient transfer learning, *arXiv preprint arXiv:2110.04366* (2021).
- [78] K. He, H. Fan, Y. Wu, S. Xie, R. Girshick, Momentum contrast for unsupervised visual representation learning, in: Proceedings of the IEEE/CVF conference on computer vision and pattern recognition, 2020, pp. 9729–9738.
- [79] A. Parnami, M. Lee, Learning from few examples: A summary of approaches to few-shot learning, *arXiv preprint arXiv:2203.04291* (2022).
- [80] D. Chicco, G. Jurman, The matthews correlation coefficient (mcc) should replace the roc auc as the standard metric for assessing binary classification, *BioData Mining* 16 (2023) 4.
- [81] J. Hancock, T. M. Khoshgoftaar, J. M. Johnson, Informative evaluation metrics for highly imbalanced big data classification, in: 2022 21st IEEE International Conference on Machine Learning and Applications (ICMLA), 2022, pp. 1419–1426. doi:10.1109/ICMLA55696.2022.00224.

## Appendix A. Overall Benchmark Results

Model	FT	LoRA <sub>r=4</sub>	LoRA <sub>r=8</sub>	LoRA <sub>r=16</sub>	VeRA <sub>r=4</sub>	VeRA <sub>r=8</sub>	VeRA <sub>r=16</sub>	BitFit	( IA ) <sup>a</sup>	LP	FFT
ResNet18	AFC	71.9 ± 9.0	71.5 ± 8.7	71.8 ± 7.8	-	-	-	72.0 ± 7.6	-	72.0 ± 7.6	<b>77.3 ± 6.8</b>
	<b>AFC<sub>m</sub></b>	23.2 ± 10.3	23.5 ± 10.6	23.5 ± 10.8	-	-	-	24.0 ± 11.5	-	38.1 ± 10.4	<b>67.2 ± 19.3</b>
	CAR	43.4 ± 6.7	40.4 ± 7.6	42.2 ± 5.5	-	-	-	41.1 ± 6.5	-	42.2 ± 14.9	<b>81.1 ± 20.0</b>
	<b>CC</b>	42.7 ± 6.0	41.9 ± 5.1	42.2 ± 6.1	-	-	-	40.2 ± 3.9	-	43.2 ± 7.3	<b>72.7 ± 21.1</b>
	NY <sub>small</sub>	15.5 ± 2.9	15.4 ± 3.0	15.4 ± 2.9	-	-	-	15.4 ± 2.9	-	40.9 ± 6.7	<b>58.4 ± 13.4</b>
	NY <sub>all</sub>	36.0 ± 2.0	35.7 ± 1.9	35.7 ± 1.9	-	-	-	45.6 ± 6.4	-	51.5 ± 2.1	<b>56.1 ± 3.2</b>
ResNet50	AFC	71.9 ± 7.6	72.2 ± 7.8	<b>73.0 ± 7.2</b>	-	-	-	72.3 ± 7.8	-	72.3 ± 7.8	72.9 ± 6.9
	<b>AFC<sub>m</sub></b>	19.0 ± 4.7	18.7 ± 4.6	19.1 ± 5.1	-	-	-	19.8 ± 5.1	-	38.4 ± 13.9	<b>48.4 ± 10.7</b>
	CAR	33.4 ± 8.0	35.0 ± 11.4	33.8 ± 9.9	-	-	-	34.4 ± 10.1	-	41.9 ± 20.6	<b>58.7 ± 22.2</b>
	CC	43.7 ± 5.8	43.8 ± 5.9	45.5 ± 9.8	-	-	-	43.9 ± 6.4	-	<b>46.5 ± 10.7</b>	41.8 ± 5.0
	NY <sub>small</sub>	13.6 ± 2.3	13.8 ± 2.3	13.7 ± 2.1	-	-	-	13.8 ± 2.1	-	36.5 ± 6.8	<b>44.6 ± 2.7</b>
	NY <sub>all</sub>	35.2 ± 2.3	35.4 ± 0.9	35.3 ± 2.0	-	-	-	35.6 ± 2.5	-	53.3 ± 3.8	<b>57.7 ± 7.0</b>
DenseNet121	AFC	72.1 ± 9.6	71.9 ± 9.6	71.9 ± 9.5	-	-	-	71.8 ± 10.1	-	71.8 ± 10.1	<b>81.9 ± 4.8</b>
	<b>AFC<sub>m</sub></b>	20.9 ± 6.7	20.9 ± 6.7	21.0 ± 6.9	-	-	-	26.4 ± 8.6	-	40.0 ± 11.1	<b>67.0 ± 24.7</b>
	<b>CAR</b>	39.2 ± 19.0	39.0 ± 19.4	39.7 ± 20.9	-	-	-	39.0 ± 18.0	-	47.4 ± 17.7	<b>83.3 ± 28.6</b>
	CC	37.6 ± 5.4	38.0 ± 6.5	43.4 ± 6.7	-	-	-	37.8 ± 6.1	-	39.6 ± 6.7	<b>69.3 ± 24.6</b>
	NY <sub>small</sub>	13.8 ± 2.1	13.8 ± 2.1	13.9 ± 2.2	-	-	-	16.6 ± 2.1	-	37.6 ± 2.9	<b>62.6 ± 17.9</b>
	NY <sub>all</sub>	33.7 ± 1.7	35.5 ± 1.4	33.8 ± 1.6	-	-	-	60.2 ± 10.2	-	51.2 ± 2.9	<b>61.7 ± 11.4</b>
MedCLIP <sub>c</sub>	AFC	77.6 ± 13.1	58.3 ± 23.1	74.7 ± 9.4	-	-	-	74.4 ± 8.9	-	74.5 ± 9.0	<b>77.1 ± 9.3</b>
	<b>AFC<sub>m</sub></b>	23.0 ± 11.9	23.8 ± 12.5	22.9 ± 11.8	-	-	-	23.6 ± 12.4	-	33.2 ± 14.7	<b>43.1 ± 11.0</b>
	CAR	38.9 ± 14.2	56.3 ± 17.0	38.7 ± 14.4	-	-	-	40.7 ± 15.2	-	42.4 ± 13.1	<b>75.8 ± 26.0</b>
	CC	42.8 ± 6.6	42.5 ± 5.6	43.2 ± 6.6	-	-	-	43.0 ± 6.4	-	38.8 ± 6.3	<b>44.1 ± 5.3</b>
	NY <sub>small</sub>	19.9 ± 12.0	20.2 ± 12.4	20.2 ± 12.4	-	-	-	20.3 ± 12.5	-	41.6 ± 8.2	<b>43.8 ± 12.9</b>
	NY <sub>all</sub>	43.5 ± 9.6	43.5 ± 9.8	43.7 ± 9.6	-	-	-	50.6 ± 6.7	-	58.4 ± 2.5	<b>59.9 ± 4.3</b>
BioMedCLIP	AFC	<b>78.3 ± 10.2</b>	77.4 ± 9.7	76.8 ± 10.0	76.9 ± 9.2	76.9 ± 10.7	76.9 ± 10.7	76.9 ± 9.6	76.6 ± 10.2	76.7 ± 9.9	73.1 ± 9.5
	<b>AFC<sub>m</sub></b>	20.3 ± 6.0	19.6 ± 4.8	19.4 ± 4.6	18.0 ± 2.5	20.4 ± 6.3	18.0 ± 2.4	20.0 ± 3.5	25.5 ± 7.6	<b>40.9 ± 10.2</b>	24.4 ± 5.3
	CAR	35.6 ± 7.8	34.6 ± 12.0	34.8 ± 11.9	35.5 ± 7.8	35.5 ± 7.8	35.8 ± 7.5	35.4 ± 12.6	<b>57.8 ± 7.2</b>	50.9 ± 13.8	43.9 ± 9.3
	CC	40.0 ± 12.8	40.0 ± 12.8	39.9 ± 12.7	40.5 ± 12.6	40.5 ± 12.7	40.4 ± 12.6	<b>43.7 ± 3.0</b>	38.3 ± 7.5	<b>43.7 ± 3.0</b>	37.7 ± 10.9
	NY <sub>small</sub>	14.6 ± 3.4	12.9 ± 2.0	12.9 ± 2.0	13.0 ± 2.1	13.0 ± 2.1	13.0 ± 2.1	12.9 ± 2.1	13.1 ± 2.3	39.2 ± 2.6	<b>54.8 ± 10.3</b>
	NY <sub>all</sub>	34.2 ± 3.8	31.7 ± 1.5	31.7 ± 1.5	32.1 ± 2.3	32.1 ± 2.3	32.1 ± 2.3	32.1 ± 2.3	33.4 ± 2.1	37.2 ± 2.3	<b>54.4 ± 2.8</b>
CLIP-Large	AFC	74.7 ± 7.6	75.0 ± 7.5	74.8 ± 7.1	<b>75.1 ± 7.6</b>	75.1 ± 7.4	<b>75.1 ± 7.4</b>	<b>75.1 ± 7.5</b>	75.0 ± 7.3	<b>75.1 ± 7.5</b>	67.4 ± 8.1
	<b>AFC<sub>m</sub></b>	24.7 ± 11.1	28.6 ± 7.4	23.5 ± 11.2	26.2 ± 10.4	23.1 ± 8.8	22.9 ± 11.5	32.7 ± 10.7	26.4 ± 10.6	<b>39.8 ± 6.0</b>	23.5 ± 9.8
	CAR	35.7 ± 13.0	56.1 ± 12.9	35.5 ± 8.4	39.4 ± 14.0	36.7 ± 13.7	36.3 ± 14.0	38.2 ± 23.2	27.8 ± 8.9	61.2 ± 16.4	<b>64.0 ± 27.7</b>
	CC	43.6 ± 8.7	42.2 ± 8.2	42.5 ± 7.2	42.4 ± 8.6	42.9 ± 9.1	42.4 ± 8.5	<b>47.8 ± 2.9</b>	41.6 ± 8.0	41.3 ± 13.7	41.0 ± 8.3
	NY <sub>small</sub>	18.8 ± 6.7	12.5 ± 1.2	12.6 ± 1.4	17.9 ± 7.3	12.7 ± 1.3	13.6 ± 0.9	17.8 ± 7.3	13.1 ± 2.0	16.3 ± 7.5	<b>43.2 ± 3.8</b>
	NY <sub>all</sub>	66.2 ± 7.5	<b>66.8 ± 9.1</b>	56.4 ± 17.7	42.4 ± 2.9	40.8 ± 2.3	34.9 ± 2.8	61.2 ± 9.2	37.6 ± 4.1	53.0 ± 4.5	62.8 ± 8.7
DINOv2 <sub>a</sub>	AFC	76.2 ± 8.1	75.7 ± 8.8	76.5 ± 7.7	76.6 ± 7.8	76.3 ± 7.7	76.3 ± 7.7	75.5 ± 8.8	76.4 ± 7.9	75.5 ± 8.8	<b>84.6 ± 7.0</b>
	<b>AFC<sub>m</sub></b>	53.2 ± 11.3	49.9 ± 16.8	<b>55.0 ± 17.2</b>	26.9 ± 13.5	24.6 ± 9.0	26.8 ± 14.9	53.1 ± 22.6	23.2 ± 10.4	41.8 ± 7.9	46.0 ± 14.5
	<b>CAR</b>	80.7 ± 16.2	54.5 ± 15.8	80.6 ± 20.9	43.6 ± 21.1	40.9 ± 14.1	42.0 ± 15.1	54.9 ± 13.4	41.5 ± 15.7	61.1 ± 13.4	69.9 ± 30.3
	CC	38.5 ± 5.3	<b>60.0 ± 17.4</b>	39.3 ± 4.8	43.4 ± 9.5	44.2 ± 8.9	44.1 ± 8.4	65.7 ± 14.3	40.9 ± 10.0	41.9 ± 6.8	36.6 ± 6.8
	<b>NY<sub>small</sub></b>	<b>52.0 ± 8.6</b>	20.4 ± 7.3	50.9 ± 9.7	20.6 ± 8.8	18.5 ± 5.6	20.4 ± 6.4	20.4 ± 5.1	13.1 ± 1.3	45.0 ± 7.5	47.4 ± 15.9
	NY <sub>all</sub>	62.1 ± 6.3	61.4 ± 6.1	60.3 ± 5.1	53.0 ± 9.9	41.8 ± 1.8	41.0 ± 2.6	61.3 ± 6.5	32.9 ± 0.8	54.7 ± 5.7	<b>71.5 ± 13.4</b>
DINOv2 <sub>b</sub>	AFC	75.1 ± 8.7	74.7 ± 8.6	75.0 ± 8.3	75.2 ± 8.3	75.3 ± 8.3	75.5 ± 8.3	74.8 ± 8.7	-	<b>77.7 ± 4.4</b>	
	<b>AFC<sub>m</sub></b>	51.0 ± 15.3	<b>56.9 ± 13.5</b>	56.5 ± 17.8	24.8 ± 8.7	26.2 ± 11.2	23.9 ± 6.8	52.9 ± 8.6	21.7 ± 7.5	44.9 ± 7.4	24.1 ± 6.7
	CAR	60.9 ± 14.5	39.2 ± 14.4	40.1 ± 11.5	48.8 ± 18.2	50.6 ± 19.4	40.9 ± 10.0	<b>65.4 ± 29.3</b>	42.1 ± 8.9	55.2 ± 14.7	44.9 ± 22.6
	<b>CC</b>	51.9 ± 6.5	63.9 ± 21.7	49.1 ± 6.3	43.9 ± 5.8	43.7 ± 5.0	43.5 ± 5.0	<b>73.3 ± 22.6</b>	40.4 ± 4.4	53.1 ± 5.6	49.2 ± 13.9
	NY <sub>small</sub>	52.5 ± 13.1	20.0 ± 5.9	<b>55.9 ± 11.1</b>	14.3 ± 4.2	17.0 ± 3.7	14.3 ± 3.9	14.5 ± 3.2	16.1 ± 2.2	43.3 ± 7.4	20.2 ± 6.0
	NY <sub>all</sub>	<b>65.5 ± 7.5</b>	64.0 ± 6.8	62.9 ± 6.8	36.1 ± 3.3	34.4 ± 2.6	34.8 ± 3.4	62.2 ± 6.4	40.5 ± 2.8	56.0 ± 7.1	50.6 ± 6.7
DINOv2 <sub>i</sub>	AFC	75.3 ± 8.5	75.8 ± 9.1	75.0 ± 8.3	75.1 ± 9.0	<b>76.3 ± 8.3</b>	75.3 ± 8.3	75.5 ± 8.3	74.8 ± 8.7	75.5 ± 8.3	63.1 ± 8.8
	<b>AFC<sub>m</sub></b>	38.6 ± 13.7	37.5 ± 10.7	38.2 ± 11.6	19.9 ± 4.8	19.9 ± 6.0	25.6 ± 9.7	30.9 ± 3.8	21.5 ± 9.2	<b>41.2 ± 6.4</b>	31.0 ± 6.9
	CAR	64.8 ± 27.7	39.3 ± 13.6	60.7 ± 23.5	42.0 ± 17.5	41.8 ± 17.6	41.8 ± 17.7	39.3 ± 10.0	41.7 ± 17.7	39.1 ± 20.8	35.1 ± 16.1
	CC	48.4 ± 5.4	47.2 ± 11.2	49.1 ± 6.3	43.2 ± 9.8	43.3 ± 9.9	43.3 ± 9.9	43.8 ± 9.5	39.0 ± 7.8	<b>50.1 ± 10.8</b>	38.7 ± 6.6
	NY <sub>small</sub>	30.5 ± 9.4	16.9 ± 8.6	30.5 ± 9.5	18.1 ± 8.1	17.5 ± 8.4	17.8 ± 8.4	16.9 ± 8.3	18.0 ± 7.1	<b>41.9 ± 9.0</b>	26.5 ± 7.7
	NY <sub>all</sub>	66.3 ± 10.4	67.8 ± 8.7	63.4 ± 9.7	35.0 ± 4.0	32.2 ± 3.9	34.7 ± 6.3	<b>68.6 ± 8.9</b>	38.3 ± 3.4	54.9 ± 4.0	46.3 ± 1.5
MedCLIP <sub>v</sub>	AFC	<b>74.8 ± 13.7</b>	56.5 ± 19.9	73.7 ± 8.7	-	-	-	75.5 ± 9.3	69.4 ± 15.1	72.2 ± 9.7	63.4 ± 7.9
	<b>AFC<sub>m</sub></b>	21.8 ± 4.3	21.0 ± 3.9	20.2 ± 4.1	-	-	-	19.6 ± 6.2	19.5 ± 4.7	<b>36.8 ± 10.2</b>	31.8 ± 7.0
	CAR	36.3 ± 24.0	36.6 ± 24.0	25.8 ± 5.6	-	-	-	23.8 ± 2.7	38.8 ± 21.3	<b>61.5 ± 15.8</b>	59.4 ± 25.5
	<b>CC</b>	<b>43.6 ± 10.4</b>	43.3 ± 10.2	39.1 ± 5.2	-	-	-	42.6 ± 8.5	36.1 ± 4.9	37.8 ± 2.5	39.4 ± 7.2
	NY <sub>small</sub>	13.8 ± 3.0	14.4 ± 3.9	14.8 ± 4.2	-	-	-	16.6 ± 5.6	14.7 ± 2.1	<b>34.5 ± 15.5</b>	29.5 ± 4.5
	NY <sub>all</sub>	34.8 ± 1.6	35.8 ± 2.5	34.8 ± 1.6	-	-	-	35.3 ± 1.4	40.4 ± 2.8	<b>52.0 ± 3.6</b>	49.3 ± 7.0
PubMedCLIP	AFC	74.6 ± 8.4	73.8 ± 8.9	74.6 ± 8.3	74.5 ± 8.4	74.9 ± 8.6	73.7 ± 9.1	75.5 ± 8.3	74.8 ± 8.7	74.9 ± 8.2	74.6 ± 8.3
	<b>AFC<sub>m</sub></b>	21.9 ± 8.2	21.2 ± 7.6	21.9 ± 7.6	22.7 ± 8.5	21.3 ± 2.9	22.6 ± 8.1	27.3 ± 10.2	20.2 ± 7.7	38.5 ± 8.9	<b>64.2 ± 22.1</b>
	CAR	33.9 ± 10.4	34.1 ± 10.7	34.1 ± 10.7	33.5 ± 10.3	33.2 ± 10.0	33.4 ± 10.2	33.1 ± 11.5	28.2 ± 7.3	53.0 ± 8.2	<b>54.0 ± 21.5</b>
	CC	39.1 ± 5.4	38.8 ± 5.3	39.0 ± 5.5	39.5 ± 5.6	39.4 ± 5.7	39.4 ± 5.6	39.3 ± 5.2	40.0 ± 5.6	43.9 ± 4.6	<b>63.2 ± 14.9</b>
	<b>NY<sub>small</sub></b>	16.6 ± 3.3	16.2 ± 4.1	16.3 ± 4.1	16.4 ± 4.3	16.2 ± 4.1	16.3 ± 4.3	16.3 ± 4.3	16.4 ± 4.3	39.3 ± 5.7	<b>76.9 ± 24.6</b>
	NY <sub>all</sub>	38.8 ± 5.6	40.2 ± 3.9	40.1 ± 3.9	38.7 ± 5.7	38.7 ± 5.7	40.1 ± 4.8	35.8 ± 2.3	51.1 ± 4.1	<b>65.1 ± 13.9</b>	

Table A.4: This table presents the **MCC** scores for all the experiments divided in two main sections by a double line, to discriminate the results obtained from CNNs (top) and FMs (bottom). Each row displays a model's performance across multiple tasks under different fine-tuning (FT) approaches, with the best fine-tuning approach per task highlighted in bold. Cells highlighted in **green** and **orange** indicate the top and second-best results, respectively, for each dataset task across all model and fine-tuning combinations.

Model	Task	FT	LoRA <sub>r=4</sub>	LoRA <sub>r=8</sub>	LoRA <sub>r=16</sub>	VeRA <sub>r=4</sub>	VeRA <sub>r=8</sub>	VeRA <sub>r=16</sub>	BitFit	IA <sup>3</sup>	LP	FFT
ResNet18	AFC	29.2 ± 8.9	27.1 ± 7.3	27.9 ± 5.7	-	-	-	30.0 ± 8.1	-	30.0 ± 8.1	<b>38.6 ± 15.5</b>	
	<b>AFC<sub>m</sub></b>	0.6 ± 12.6	1.7 ± 12.8	0.4 ± 12.2	-	-	-	12.8 ± 3.8	-	5.9 ± 10.1	<b>45.6 ± 25.3</b>	
	CAR	2.7 ± 8.2	7.1 ± 15.2	7.1 ± 15.2	-	-	-	24.7 ± 0.0	-	11.1 ± 21.2	<b>45.7 ± 39.3</b>	
	<b>CC</b>	-1.4 ± 14.8	1.1 ± 9.2	2.1 ± 7.2	-	-	-	6.5 ± 0.8	-	3.0 ± 12.3	<b>46.8 ± 25.2</b>	
	NV <sub>small</sub>	2.2 ± 3.7	3.0 ± 4.4	2.8 ± 4.5	-	-	-	13.2 ± 0.0	-	26.6 ± 13.2	40.8 ± 13.9	
	NV <sub>all</sub>	-0.1 ± 2.8	-1.3 ± 3.0	-1.0 ± 2.9	-	-	-	1.4 ± 0.8	-	20.7 ± 2.5	<b>25.2 ± 4.0</b>	
ResNet50	AFC	29.2 ± 5.5	30.0 ± 8.0	29.1 ± 11.5	-	-	-	28.4 ± 8.4	-	28.4 ± 8.4	<b>30.8 ± 6.8</b>	
	<b>AFC<sub>m</sub></b>	-3.7 ± 3.5	-3.1 ± 5.6	-3.5 ± 8.7	-	-	-	12.8 ± 3.8	-	10.4 ± 8.2	<b>25.0 ± 14.3</b>	
	CAR	12.5 ± 26.7	10.8 ± 23.5	8.6 ± 32.2	-	-	-	24.7 ± 0.0	-	4.4 ± 25.8	<b>40.2 ± 25.9</b>	
	<b>CC</b>	2.2 ± 19.3	-2.7 ± 11.5	<b>8.9 ± 16.0</b>	-	-	-	6.5 ± 0.8	-	3.4 ± 20.9	3.7 ± 3.8	
	NV <sub>small</sub>	0.3 ± 2.8	1.6 ± 4.2	0.6 ± 5.2	-	-	-	13.2 ± 0.0	-	8.2 ± 6.5	<b>22.6 ± 6.2</b>	
	NV <sub>all</sub>	-3.4 ± 2.5	-1.1 ± 1.9	-2.1 ± 3.8	-	-	-	1.1 ± 0.0	-	20.1 ± 2.8	<b>27.1 ± 7.8</b>	
DenseNet121	AFC	35.2 ± 5.8	31.3 ± 5.5	30.6 ± 5.4	-	-	-	32.1 ± 7.3	-	32.1 ± 7.3	<b>42.1 ± 14.9</b>	
	<b>AFC<sub>m</sub></b>	4.1 ± 12.5	4.5 ± 12.1	3.8 ± 12.4	-	-	-	12.8 ± 3.8	-	20.1 ± 4.6	<b>51.8 ± 11.1</b>	
	<b>CAR</b>	4.1 ± 22.5	-3.6 ± 24.8	2.8 ± 21.4	-	-	-	24.7 ± 0.0	-	18.7 ± 26.2	<b>70.4 ± 36.8</b>	
	CC	-3.4 ± 10.5	-0.1 ± 8.7	2.3 ± 15.1	-	-	-	8.0 ± 2.9	-	-1.5 ± 9.4	<b>32.5 ± 44.0</b>	
	NV <sub>small</sub>	-1.1 ± 3.6	-1.4 ± 4.9	-1.3 ± 2.7	-	-	-	13.2 ± 0.0	-	21.2 ± 8.5	43.9 ± 24.1	
	NV <sub>all</sub>	-0.3 ± 0.9	-0.4 ± 2.0	0.1 ± 1.4	-	-	-	27.8 ± 18.5	-	20.9 ± 3.2	<b>33.1 ± 13.8</b>	
MedCLIP <sub>c</sub>	AFC	26.8 ± 10.7	2.6 ± 17.9	33.8 ± 10.5	-	-	-	33.7 ± 9.3	-	33.7 ± 8.8	<b>39.4 ± 8.7</b>	
	<b>AFC<sub>m</sub></b>	-1.9 ± 12.9	-1.5 ± 12.8	-1.2 ± 12.9	-	-	-	13.4 ± 4.7	-	17.5 ± 11.2	<b>18.1 ± 8.0</b>	
	CAR	14.8 ± 22.2	31.9 ± 22.0	9.3 ± 23.8	-	-	-	28.9 ± 9.5	-	19.2 ± 20.0	<b>49.0 ± 24.2</b>	
	CC	1.6 ± 10.9	1.5 ± 12.0	3.1 ± 12.4	-	-	-	4.0 ± 16.8	-	7.4 ± 2.4	<b>8.5 ± 4.3</b>	
	NV <sub>small</sub>	4.1 ± 12.3	4.3 ± 12.5	4.2 ± 12.6	-	-	-	15.2 ± 4.6	-	21.4 ± 5.5	<b>29.5 ± 10.7</b>	
	NV <sub>all</sub>	0.6 ± 2.8	0.4 ± 2.9	0.6 ± 2.7	-	-	-	16.3 ± 10.6	-	19.9 ± 10.3	<b>30.9 ± 5.4</b>	
BioMEdCLIP	AFC	<b>38.9 ± 12.0</b>	38.5 ± 12.6	37.1 ± 13.3	38.5 ± 12.3	37.4 ± 15.6	36.1 ± 13.5	36.8 ± 12.2	38.7 ± 11.8	34.3 ± 10.7		
	<b>AFC<sub>m</sub></b>	8.3 ± 7.9	6.9 ± 9.6	-11.8 ± 6.9	1.4 ± 13.3	-11.9 ± 6.8	<b>12.8 ± 3.8</b>	9.9 ± 8.4	10.6 ± 14.9	<b>12.8 ± 3.8</b>		
	CAR	-11.5 ± 35.6	9.9 ± 21.7	9.9 ± 21.7	-11.5 ± 35.6	-11.5 ± 35.6	24.7 ± 0.0	<b>40.8 ± 2.8</b>	13.9 ± 26.1	22.8 ± 11.8		
	CC	-4.7 ± 21.4	-4.7 ± 21.4	-4.7 ± 21.4	-3.3 ± 18.1	-3.3 ± 18.1	3.2 ± 12.1	-0.2 ± 15.2	-0.8 ± 9.3	<b>6.8 ± 1.3</b>		
	<b>NV<sub>small</sub></b>	7.3 ± 6.8	1.5 ± 8.1	1.5 ± 8.1	1.3 ± 8.2	1.3 ± 8.2	1.3 ± 8.2	0.5 ± 8.0	0.5 ± 8.0	<b>21.2 ± 16.5</b>	1.2 ± 1.7	
	NV <sub>all</sub>	-2.3 ± 6.3	-8.6 ± 3.1	-8.7 ± 3.1	-4.3 ± 3.6	-4.4 ± 3.6	-4.3 ± 3.6	-0.3 ± 1.6	2.2 ± 3.6	<b>29.7 ± 3.7</b>	18.5 ± 5.5	
CLIP-Large	AFC	30.1 ± 5.8	31.9 ± 10.3	<b>33.9 ± 8.3</b>	31.3 ± 6.9	31.9 ± 9.3	33.5 ± 9.0	30.1 ± 8.2	33.5 ± 9.0	17.5 ± 13.2		
	<b>AFC<sub>m</sub></b>	12.8 ± 3.8	10.2 ± 4.7	5.4 ± 10.3	9.6 ± 9.6	5.1 ± 10.9	4.3 ± 11.1	12.8 ± 3.8	4.3 ± 7.5	<b>13.0 ± 16.1</b>	12.8 ± 3.8	
	CAR	4.3 ± 29.8	27.6 ± 6.6	5.2 ± 18.3	2.0 ± 28.1	5.3 ± 30.8	24.7 ± 0.0	-5.8 ± 29.2	24.6 ± 14.4	<b>28.2 ± 25.3</b>		
	CC	-6.4 ± 15.1	-4.6 ± 10.7	-7.5 ± 10.4	-7.1 ± 6.2	-1.0 ± 13.7	-1.1 ± 13.0	3.5 ± 6.4	3.3 ± 12.6	2.6 ± 19.4	<b>6.5 ± 0.8</b>	
	NV <sub>small</sub>	13.2 ± 0.6	-4.8 ± 7.5	-4.3 ± 7.2	5.5 ± 11.7	1.5 ± 4.5	-3.5 ± 6.0	13.2 ± 0.0	0.5 ± 8.0	<b>21.2 ± 16.5</b>	1.2 ± 1.7	
	NV <sub>all</sub>	39.7 ± 8.9	<b>43.5 ± 10.2</b>	32.5 ± 23.6	1.2 ± 0.8	1.3 ± 2.0	-1.1 ± 4.5	28.5 ± 19.7	-0.3 ± 5.2	21.7 ± 5.1	33.7 ± 9.1	
DINOv2 <sub>a</sub>	AFC	36.5 ± 6.1	33.3 ± 10.1	36.3 ± 6.7	36.5 ± 9.2	36.0 ± 6.9	36.0 ± 6.9	34.2 ± 10.6	34.3 ± 7.2	34.2 ± 10.6	<b>49.6 ± 13.8</b>	
	<b>AFC<sub>m</sub></b>	<b>32.5 ± 20.3</b>	16.7 ± 15.4	26.0 ± 23.5	8.5 ± 8.5	12.8 ± 3.8	5.0 ± 12.3	22.0 ± 10.2	3.6 ± 11.2	15.3 ± 13.8	28.2 ± 13.7	
	<b>CAR</b>	<b>77.2 ± 16.4</b>	27.6 ± 6.6	68.7 ± 28.8	14.8 ± 22.1	14.8 ± 22.1	11.5 ± 19.5	14.8 ± 22.1	12.3 ± 36.4	28.6 ± 40.8		
	CC	-2.6 ± 8.6	37.7 ± 27.6	-3.5 ± 11.3	1.1 ± 11.1	8.1 ± 5.6	7.2 ± 6.8	<b>39.2 ± 23.8</b>	0.9 ± 11.8	1.8 ± 5.6	2.2 ± 9.3	
	<b>NV<sub>small</sub></b>	<b>41.3 ± 14.1</b>	13.2 ± 0.0	30.9 ± 20.3	5.0 ± 7.8	9.3 ± 6.7	9.9 ± 4.7	13.2 ± 0.0	-5.7 ± 5.4	31.4 ± 5.4	33.9 ± 19.6	
	NV <sub>all</sub>	35.9 ± 7.2	34.6 ± 6.7	35.2 ± 6.2	21.6 ± 15.0	4.2 ± 1.8	3.1 ± 3.4	35.2 ± 8.2	-2.1 ± 1.6	26.1 ± 6.4	<b>44.6 ± 18.5</b>	
DINOv2 <sub>b</sub>	AFC	34.7 ± 8.2	<b>36.1 ± 8.7</b>	34.0 ± 5.8	34.1 ± 9.5	32.6 ± 7.5	32.6 ± 7.5	35.0 ± 5.9	33.0 ± 9.8	35.0 ± 5.9	35.9 ± 11.3	
	<b>AFC<sub>m</sub></b>	<b>30.0 ± 25.0</b>	28.2 ± 16.6	26.2 ± 22.1	14.7 ± 7.8	7.7 ± 7.3	13.1 ± 6.9	19.8 ± 10.5	5.7 ± 8.5	15.9 ± 12.8	12.8 ± 3.8	
	CAR	45.4 ± 2.1	24.7 ± 0.0	18.6 ± 19.9	2.8 ± 24.4	28.5 ± 30.0	22.0 ± 22.0	<b>47.0 ± 46.5</b>	22.0 ± 22.0	18.1 ± 29.1	20.7 ± 9.1	
	CC	14.9 ± 15.3	34.0 ± 26.6	10.8 ± 16.0	10.1 ± 5.5	11.0 ± 5.9	11.0 ± 5.9	4.9 ± 8.5	0.3 ± 9.0	<b>46.9 ± 29.6</b>	6.2 ± 9.1	3.7 ± 12.1
	NV <sub>small</sub>	35.0 ± 21.0	13.2 ± 0.0	<b>37.5 ± 21.9</b>	1.9 ± 10.4	7.7 ± 11.7	4.6 ± 12.0	13.2 ± 0.0	-4.8 ± 11.0	24.5 ± 11.4	13.2 ± 0.0	
	NV <sub>all</sub>	<b>40.3 ± 8.9</b>	35.7 ± 8.8	34.4 ± 8.5	1.8 ± 1.0	0.3 ± 1.8	-2.6 ± 7.1	35.5 ± 8.6	0.8 ± 1.8	25.9 ± 9.3	15.1 ± 15.4	
DINOv2 <sub>i</sub>	AFC	36.6 ± 11.0	31.8 ± 13.7	34.0 ± 5.8	32.0 ± 14.5	<b>38.8 ± 11.5</b>	32.6 ± 7.5	35.0 ± 5.9	33.0 ± 9.8	35.0 ± 5.9	35.9 ± 11.3	
	<b>AFC<sub>m</sub></b>	14.9 ± 3.7	<b>15.5 ± 4.7</b>	15.2 ± 10.1	11.1 ± 3.5	12.8 ± 3.8	2.9 ± 9.9	12.8 ± 3.8	-2.9 ± 12.3	13.2 ± 12.1	11.8 ± 5.6	
	CAR	<b>37.2 ± 20.7</b>	32.2 ± 16.8	34.2 ± 14.5	32.2 ± 16.8	32.2 ± 16.8	24.7 ± 0.0	-32.2 ± 16.8	8.6 ± 23.7	6.8 ± 33.1		
	CC	8.3 ± 5.7	6.5 ± 0.8	10.8 ± 16.0	10.1 ± 5.5	11.0 ± 5.9	6.8 ± 6.7	4.0 ± 10.3	<b>15.5 ± 12.9</b>	4.3 ± 5.5		
	NV <sub>small</sub>	13.2 ± 0.6	7.4 ± 9.0	13.2 ± 0.0	9.4 ± 8.4	9.4 ± 8.4	10.0 ± 9.1	13.2 ± 0.0	-9.6 ± 14.2	<b>16.9 ± 8.6</b>	13.2 ± 0.0	
	NV <sub>all</sub>	39.6 ± 10.5	44.6 ± 11.2	11.1 ± 1.0	-0.9 ± 4.4	-0.0 ± 6.9	<b>46.4 ± 9.5</b>	1.7 ± 1.7	25.6 ± 7.2	11.0 ± 4.4		
MedCLIP <sub>v</sub>	AFC	28.7 ± 4.1	4.2 ± 12.5	<b>34.8 ± 4.8</b>	-	-	-	27.7 ± 16.3	31.7 ± 17.0	27.3 ± 16.4	18.3 ± 9.2	
	<b>AFC<sub>m</sub></b>	4.7 ± 7.5	7.0 ± 7.1	8.3 ± 7.5	-	-	-	12.8 ± 3.8	-8.6 ± 9.5	<b>16.9 ± 20.4</b>	12.8 ± 3.8	
	CAR	14.8 ± 22.1	14.8 ± 22.1	10.3 ± 19.8	-	-	-	24.7 ± 0.0	-11.2 ± 21.5	<b>35.2 ± 10.4</b>	29.1 ± 24.5	
	CC	<b>7.7 ± 2.3</b>	6.1 ± 0.9	1.4 ± 7.2	-	-	-	5.1 ± 10.3	-6.7 ± 8.3	1.5 ± 7.0	-3.6 ± 9.2	
	NV <sub>small</sub>	0.7 ± 7.7	3.2 ± 9.4	2.1 ± 7.3	-	-	-	13.2 ± 0.0	-4.5 ± 8.7	<b>22.1 ± 11.3</b>	10.1 ± 6.9	
	NV <sub>all</sub>	-1.5 ± 2.1	0.2 ± 3.2	-1.3 ± 1.8	-	-	-	0.8 ± 2.1	-1.2 ± 0.6	<b>24.2 ± 4.7</b>	11.1 ± 13.6	
PubMedCLIP	AFC	33.6 ± 6.4	27.0 ± 12.5	33.9 ± 6.3	33.9 ± 5.7	29.5 ± 5.6	28.4 ± 6.5	34.6 ± 6.6	30.9 ± 7.7	34.6 ± 6.6	<b>47.4 ± 13.7</b>	
	<b>AFC<sub>m</sub></b>	2.9 ± 8.2	6.2 ± 10.2	5.9 ± 10.1	2.6 ± 11.8	0.7 ± 13.6	2.6 ± 11.8	12.8 ± 3.8	-6.7 ± 9.9	8.2 ± 11.4	44.9 ± 27.1	
	CAR	-4.2 ± 26.4	-1.7 ± 25.0	-0.5 ± 24.7	-4.2 ± 26.4	-4.2 ± 26.4	24.7 ± 0.0	-7.2 ± 31.1	24.7 ± 0.0	25.3 ± 31.1		
	CC	-0.3 ± 7.8	1.2 ± 6.2	1.2 ± 6.2	1.2 ± 6.2	1.2 ± 6.2	6.5 ± 0.8	-7.1 ± 10.3	7.6 ± 11.6	17.8 ± 16.4		
	<b>NV<sub>small</sub></b>	-0.6 ± 10.7	1.4 ± 10.5	1.4 ± 10.5	1.6 ± 10.6	1.4 ± 10.5	1.6 ± 10.6	13.2 ± 0.0	2.0 ± 5.8	21.1 ± 9.0	<b>65.0 ± 25.2</b>	
	NV <sub>all</sub>	2.0 ± 4.1	3.3 ± 2.3	3.2 ± 2.3	1.0 ± 4.1	1.0 ± 4.1	1.1 ± 0.0	-1.5 ± 3.7	18.0 ± 4.2	38.4 ± 17.1		

Table A.5: This table presents the **PR-AUC** scores for all the experiments divided in two main sections by a double line, to discriminate the results obtained from CNNs (top) and FMs (bottom). Each row displays a model's performance across multiple tasks under different fine-tuning approaches, with the best fine-tuning approach per task highlighted in **bold**. Cells highlighted in **green** and **orange** indicate the top and second-best results, respectively, for each dataset task across all model and fine-tuning combinations.